How Snow Aggregate Ellipsoid Shape and Orientation Variability Affects Fall Speed and Self-Aggregation Rates

EDWIN L. DUNNAVAN[a,b]

[a] *Cooperative Institute for Mesoscale Meteorological Studies, University of Oklahoma, Norman, Oklahoma*
[b] *NOAA/OAR/National Severe Storms Laboratory, Norman, Oklahoma*

(Manuscript received 28 April 2020, in final form 1 October 2020)

ABSTRACT: Snow aggregate shapes and orientations have long been known to exhibit substantial variability. Despite this observed variability, most weather and climate prediction models use fixed power-law functions that deterministically map particle size to mass and fall speed. As such, integrated quantities like precipitation and self-aggregation rates currently ignore nonlinear effects resulting from variation in shape and orientation for aggregates of the same size. This study therefore develops an analytic framework that couples an empirically based bivariate distribution of ellipsoid shapes to classical hydrodynamic theory so as to capture an appropriate dispersion of masses, projected areas, and fall speeds for an assumed size distribution. For a fixed aggregate size, shape variations produce approximately $\pm 0.13\ \mathrm{m\ s^{-1}}$ standard deviation of fall speed which increases the mass flux fall speed dispersion by more than 100% over traditional microphysics models. This increased fall speed dispersion results predominantly from shape-induced mass dispersion whereas orientation and drag dispersion play a lesser role. Shape variations can increase mass- and reflectivity-weighted fall speeds by up to 60% of traditional models whereas self-aggregation rates can increase by a factor of 100 for very small slope parameters. This implies that aggregate shape variations effectively forestall the theorized onset of fall speed distribution narrowing and subsequent quenching of the aggregation process. As a result, it is likely that secondary ice formation is necessary to prevent an ever decreasing slope parameter. The mathematical theory presented in this study is used to develop simple correction factors for snow forecast and climate models.

KEYWORDS: Atmosphere; Snow; Winter/cool season; Cloud microphysics; Spectral analysis/models/distribution; Cloud parameterizations

1. Introduction

A delicate balance of gravitational and drag forces governs the terminal fall speed of snowflake aggregates. The resulting distribution of aggregate fall speeds and masses are particularly important for predicting surface precipitation rates and cloud longevity. However, the variety of aggregate shapes complicates this balance because they affect both forces simultaneously: particle masses directly dictate the gravitational force whereas the spatial distribution of this mass (often characterized by a quantity called the area ratio) dictates the aggregate's drag. That snow aggregate shapes affect *both* these quantities suggests potentially substantial nonlinearities in terminal fall speed calculations which, in turn, affects the growth processes themselves. Various aggregate orientations resulting from fall behavior such as oscillations, tumbling, or swirling (Kajikawa 1982) compound these nonlinear relationships between shape and fall speed by further altering drag.

Most current numerical weather prediction (NWP) and climate models characterize this balance by relating aggregate size to mass and fall speed using one-to-one power-law relations. While environmental corrective factors are often used in conjunction with these power-law functions, integral moments of the particle size distribution (PSD) are heavily weighted by both the chosen fall speed–size (v_t–D) and mass–size (M–D) power-law parameters. Therefore, predicted integrated quantities that depend upon both mass and fall speed (e.g., precipitation rates) are accurate only if correlation terms between both microphysical quantities are relatively small. There is however some evidence that these nonlinear correlation terms can produce profound effects on bulk quantities. For example, Passarelli and Srivastava (1979) used an assumed rectangular probability distribution of fall speed dispersion about mean particle mass and density to examine the potential effects on the snow self-aggregation kernel. They found that this introduction of fall speed variation dramatically increased the collection kernel for the larger end of the size spectrum. A later study by Böhm (1992) reiterated these results but provided the following sober account on its validity: "These highly idealizing assumptions were suitable for a first investigation of the significance of these effects, but they obviously are not very accurate." Multiple studies (e.g., Passarelli and Srivastava 1979; Sasyo and Matsuo 1980; Böhm 1992; Schmitt et al. 2019) prescribe a fixed probability distribution of aggregate fall speeds about size (mass). Assuming a strictly one-to-one mass and fall speed relationship permits analytical treatment within the collection integrals but does not take into account the positive correlation between mass and fall speed variations. Ignoring the appropriate correlations between mass, projected

Supplemental information related to this paper is available at the Journals Online website: https://doi.org/10.1175/JAS-D-20-0128.s1.

Corresponding author: Edwin Lee Dunnavan, edwin.dunnavan@noaa.gov, dunnavel@ou.edu

DOI: 10.1175/JAS-D-20-0128.1

area, and fall speed necessarily eliminates potentially important nonlinear terms that influence particle fluxes and collection rates. Radar studies have generally shown that nonlinear microphysical relationships between correlated variables are important for predicting snowfall rates (Wood et al. 2015). However, there is currently no encompassing mathematical theory capable of incorporating an appropriate dispersion of particle properties so as to capture their correct correlations, variations, and nonlinear relationships while maintaining an analytic framework.

In theory, the semiempirical methodology of Böhm (1989) and others can be used to mathematically and synergistically connect particle properties such as size, shape, and density to fall speed. However, the sheer variety of different aggregate forms complicates the notion of shape and density for a given aggregate and how these factors should influence fall speed. For microphysical quantities such as snow precipitation rates and radar quantities such as Doppler velocity, mass directly appears in the integration kernels as well as in the characterization of fall speed, thereby further increasing nonlinear complexity. Although various semiempirical studies employ the same general drag parameterization approach, the specifics of each study give slightly different forms and parameters that dictate the fall speed–dimensional power-law parameters.

Recently, ground-based observations have provided a much better understanding of snow aggregate shape and orientation distributions. For instance, the Multi-Angle Snowflake Camera (MASC) imager (Garrett et al. 2015) permits multiple viewing angles of the same particle. This can help mitigate orientation uncertainties that obfuscate shape estimation. Garrett et al. (2015) used the MASC to develop distributions of aggregate shapes, sizes, fall speeds, and orientations. They discovered that orientations, in particular, exhibit a much broader distribution that becomes even broader with increasing turbulence than previously thought. More recently, Jiang et al. (2019) used machine learning techniques to estimate aggregate shapes and orientations from the MASC multiple viewing angles. To do this, Jiang et al. (2019) used triaxial ellipsoids as proxies for aggregate shapes and found that a bivariate beta distribution of ellipsoid aspect ratios could capture the full observed distribution. This distribution presents a very different conception of aggregate shapes than the spherical (e.g., Brandes et al. 2007) and oblate (e.g., Hogan et al. 2012) assumptions given in previous observational studies. Dunnavan et al. (2019) extended the work of Jiang et al. (2019) so as to provide ellipsoid fits to Monte Carlo simulated aggregates and discovered that these simulated aggregates also assume the same type of bivariate beta distribution form as estimated from the MASC observations. Through a series of Monte Carlo simulations, Dunnavan et al. (2019) were able to explore ellipsoidal and fractal sensitivities of generated aggregates to the shape of their various constituent particles.

Traditional power-law approaches assume that particle size (often maximum dimension or sphere equivalent-volume diameter) follows an inverse-exponential or gamma distribution. Properties such as shape, mass, and fall speed are dictated in terms of a power law according to this size. A simple substitution of variables in the assumed size distribution using these power-law functions rescales the distribution in the form of a Weibull distribution for inverse-exponential size distributions or the Amoroso or generalized gamma distribution for gamma size distributions. As a result, traditional approaches either explicitly or implicitly incorporate ice particle shape in calculations by representing aspect ratios as power-law functions of size and the power-law transformation into other variables (e.g., mass or fall speed) leads to a more general distribution function within the gamma family. However, the ground-based observations shown in Jiang et al. (2019) and Dunnavan et al. (2019) suggest that snow aggregate shapes are only a weak function of size and that a separate distribution function, the bivariate beta distribution, can appropriately capture its functional form. A fundamental question is, therefore, What *would* be the distribution form for a variable like mass or fall speed with gamma distributed size and bivariate beta distributed shape? Furthermore, how would distribution moments change accordingly, and would these moments affect highly nonlinear bulk properties such as snow precipitation rates (i.e., mass-weighted fall speed) or self-aggregation of the second mass moment (reflectivity)?

This study answers these questions by establishing a mathematical foundation for convolving size and shape when describing snow aggregate properties. These additional mathematical tools generalize the conventional gamma distribution power-law transformations with the use of Mellin integral transforms. While the mathematical basis for these integral transforms is well established, the resulting general distribution function, Fox's H function, appears to be rather esoteric even within the mathematics community. Moreover, H-function behavior, properties, and various notations will undoubtably appear alien and confusing to those unfamiliar with its use. Therefore, the mathematical details of the H function are presented in the online supplementary materials section. This deep mathematical analysis can, in theory, be used in conjunction with observed distributions from instruments such as the MASC (e.g., Garrett et al. 2015), thus giving an additional level of comparison between observations and microphysical models. This new mathematical framework also provides a vehicle for connecting various particle properties together when developing microphysical parameterizations. While these transforms can lead to more complicated expressions for distribution functions of particular variables, the underlying moments of an H-function distribution are still given in terms of gamma function ratios as with the gamma distribution. Therefore, the moments themselves still exist within the conventional microphysics framework and would not severely complicate implementation into microphysics models.

2. Theory and methodology

a. Distribution convolutions and product moments

The gamma distribution as presented within cloud microphysics literature is often shown in one of two different forms:

$$n(D) = N_0 D^{\mu} \exp(-\Lambda D), \tag{1a}$$

$$n(D) = \frac{N_i}{\Gamma(\nu)} \frac{1}{D_n} \left(\frac{D}{D_n}\right)^{\nu-1} \exp\left(-\frac{D}{D_n}\right), \quad (1b)$$

where Eq. (1a) often describes observed size distributions (e.g., Heymsfield et al. 2002a; McFarquhar et al. 2007) and Eq. (1b) often describes microphysical model size distributions (e.g., Walko et al. 1995; Harrington et al. 2013). The term Λ is commonly referred to as the ''slope'' parameter whereas D_n is sometimes called the ''characteristic diameter'' (all variables used throughout this paper are also defined in the appendix). Observations often use Eq. (1a) when determining parameters N_0 and Λ and sometimes μ through the use of nonlinear least squares fitting or method-of-moment fitting (see McFarquhar et al. 2007). This means that the total number mixing ratio of ice particles, N_i, is a free parameter that is dictated by the combination of fitted parameters N_0, Λ, and μ. Microphysics models, on the other hand, often use predictive equations for this number mixing ratio. Therefore, the scaled form of Eq. (1b) permits simpler expressions for the various moments of the size distribution. These moments relate to fundamental quantities such as ice water content (IWC), precipitation rates (mass flux), or reflectivity (assuming Rayleigh scattering). Throughout this study $\mu = 0$ as a way to simplify the analysis and sensitivity tests. $\mu = 0$ is often observed in nature but can deviate from this value (e.g., Brandes et al. 2007) which can influence how mass is distributed across the size spectrum. Further studies would be required to fully investigate these other factors.

For this work, triaxial ellipsoids represent ice particle aggregates where the ellipsoid semimajor dimension a follows a gamma distribution and the ellipsoid aspect ratios, $\varphi_{ba} \equiv b/a$ and $\varphi_{ca} \equiv c/a$, follow a bivariate beta distribution where $a \geq b \geq c$. The bivariate beta distribution is given in Dunnavan et al. (2019) as

$$\tilde{n}(\varphi_{ba}, \varphi_{ca}) = \frac{1}{B(\alpha_{ba}, \beta_{ba}) B(\alpha_{ba} + \beta_{ba}, \beta_{cb})} \varphi_{ca}^{\alpha_{ba}+\beta_{ba}-1} \times (\varphi_{ba} - \varphi_{ca})^{\beta_{cb}-1} \varphi_{ba}^{-\beta_{ba}-\beta_{cb}} (1 - \varphi_{ba})^{\beta_{ba}-1}, \quad (2)$$

where α_{ba}, β_{ba}, and β_{cb} are distribution parameters and $B(x, y)$ is the beta function. The MASC data from Dunnavan et al. (2019) suggest that $\alpha_{ba} = 6.9793$, $\beta_{ba} = 4.3502$, and $\beta_{cb} = 5.3437$ for ground-based snow. These values will be used throughout this work to represent such snowfall. Product moments of this bivariate distribution are

$$\langle \varphi_{ba}^m \varphi_{ca}^n \rangle = \frac{B(m + n + \alpha_{ba}, \beta_{ba}) B(n + \alpha_{ba} + \beta_{ba}, \beta_{cb})}{B(\alpha_{ba}, \beta_{ba}) B(\alpha_{ba} + \beta_{ba}, \beta_{cb})}. \quad (3)$$

The general form for an algebraic combination of microphysical variables is given by

$$\xi = \alpha_\xi a^{\zeta_a} \varphi_{ba}^{\zeta_{ba}} \varphi_{ca}^{\zeta_{ca}}, \quad (4)$$

where ξ is a microphysical quantity that depends on a, φ_{ba}, and φ_{ca}. For example, aggregate ellipsoid volumes can be described as $V_e = (4/3)\pi a^3 \varphi_{ba} \varphi_{ca}$, where $\zeta_a = 3$ and $\zeta_{ba} = \zeta_{ca} = 1$. Distribution moments of $n(\xi)$ are a product of Eq. (3) and the traditional gamma distribution moments of $n(a)$. The general convolved distributions for ξ can be expressed in terms of Fox's H function (Fox 1961) where each form is derived and explained in detail within the supplementary materials section. Equation (4) can be used in the same way as traditional M–D and v_t–D relationships. The following section derives new ellipsoid power-law parameters in Eq. (4) that incorporate a dispersion of shape and orientation. It is important to realize that ellipsoids only represent a mathematically convenient proxy for aggregate shapes and densities which permit an already established semiempirical methodology. Additional details and uncertainties associated with the impact of morphology, turbulence, and other factors on fall speed require a special study and is therefore outside the scope of the current paper.

b. *Fall speed*

Much of the theory and mathematical treatment of hydrometeor fall speed can be attributed to a series of papers by Hannes Böhm (Böhm 1989, 1992). In these papers, hydrometeors are imagined as reduced-density spheroids with terminal fall speeds that are governed by the balance of gravitational and drag forces. The theory itself is semiempirical with the drag force component based off of the theory and experiments of spheres conducted by Abraham (1970). Further modification of Böhm's work has been developed by Mitchell (1996), Heymsfield et al. (2002a), Khvorostyanov and Curry (2002), Mitchell and Heymsfield (2005), Khvorostyanov and Curry (2005), and Heymsfield and Westbrook (2010). These additional studies generalized the original equations of Böhm (1989) such that particles were not necessarily treated as spheroids. This allowed Mitchell (1996), Mitchell and Heymsfield (2005), and Heymsfield and Westbrook (2010) to parameterize fall speed using in situ or laboratory derived power-law relations for the particle projected area A_{part}. The following is a further extension of these works but with the introduction of a bivariate ellipsoid shape distribution based on observed aggregates (Dunnavan et al. 2019; Jiang et al. 2019).

The general terminal fall speed equation is given in Böhm (1989) as

$$v_t = \frac{1}{2} \frac{\eta_a}{\rho_a} \sqrt{\frac{\pi}{A_{\text{proj}}}} N_{\text{Re}}, \quad (5)$$

where N_{Re} is the Reynolds number, η_a is the dynamic viscosity, ρ_a is the air density, and A_{proj} is the ellipsoidal shell projected area onto the horizontal x–y plane (see Fig. 1 from Böhm 1989). For this comparison study, aggregates are imagined as spheres and ellipsoids where the effective density decreases as a function of size. A common interpretation of a reduced-density sphere is that of a fractal object where the chosen length scale is the sphere's maximum dimension D or radius R (cf. Heymsfield et al. 2002a,b). This interpretation, for instance, is described in Blumenfeld and Mandelbrot (1997) where the fractal object is envisioned to be enclosed by a sphere with the same maximum dimension as that of the object

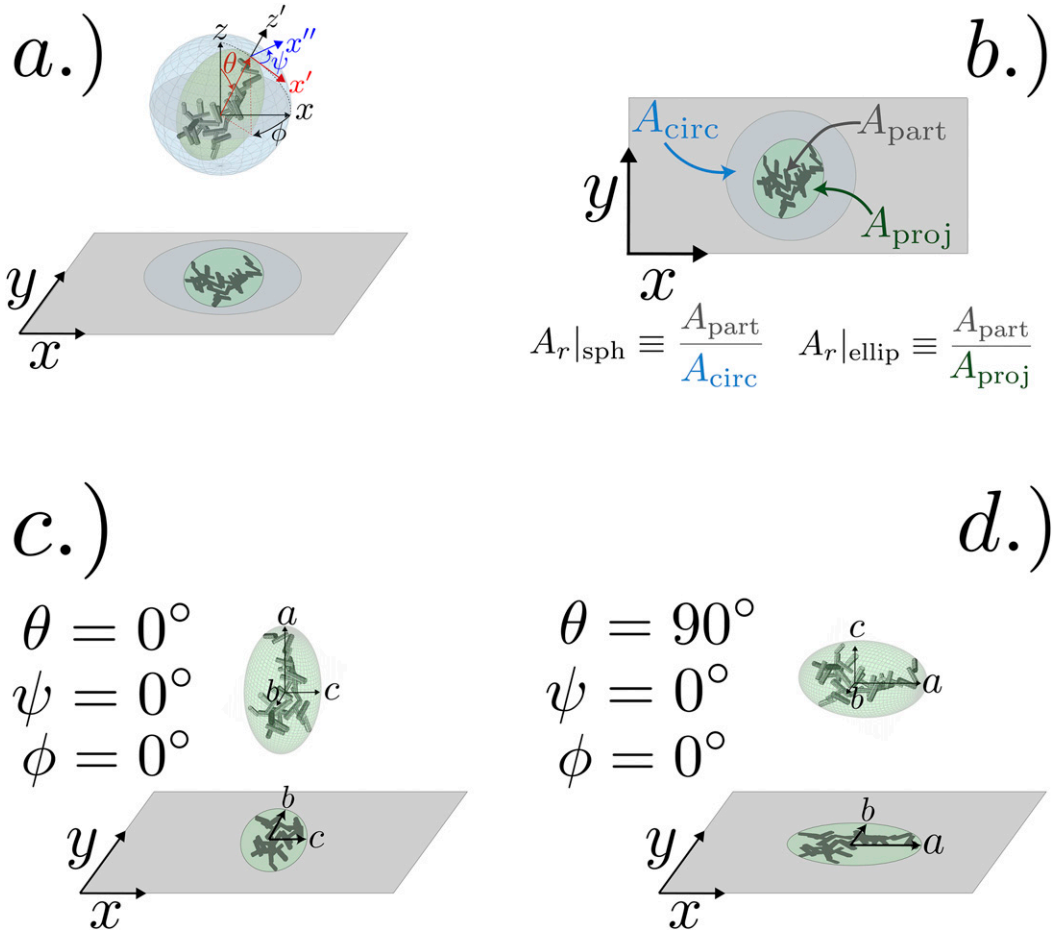

FIG. 1. Geometry for projecting ellipsoid area and area ratios. (a) General Euler angle rotation convention following *Z*–*Y*–*Z* rotations. (b) Top-down *x*–*y* plane projection for the general case of projected particle area A_{part} (gray area), projected circle A_{circ}, (blue circle), and projected ellipse area A_{proj} (green ellipse). Area ratios are defined by the ratio of A_{part} to each projected areas as shown. Notice that A_{circ} is defined in terms of the particle maximum dimension D rather than the projected maximum dimension. (c) Minimum $A_{\text{proj}} = \pi bc = \pi a^2 \varphi_{ba} \varphi_{ca}$ case. (d) Maximum $A_{\text{proj}} = \pi ab = \pi a^2 \varphi_{ba}$ case. Aggregate image in all four panels adapted from Fig. 12 in Westbrook et al. (2008).

itself. The fractal dimension β_{m_s} then describes how the particle mass scales according to D or R assuming that the fractal object is self-similar at various scales, $0 < r \leq R$. These dual views of aggregates as either fractals or reduced-density spheres are used interchangeably throughout this study with these perspectives in mind where the subscript s represents ''sphere.'' The concept of reduced-density ellipsoids, as denoted by the subscript e, therefore extends current approaches by taking the reduced-density sphere parameterizations for aggregate mass and projected area and simply introduces additional aspect ratio terms as correction factors.

For general triaxial ellipsoid shapes, both N_{Re} and A_{proj} must be reformulated because shape and orientation implicitly alter these parameters. To calculate A_{proj}, the ellipsoid is first aligned with its two semiminor axes, b and c, along the *x*–*y* plane (Fig. 1c) where a, b, and c are initially along the z, y, and x axes, respectively. Then, three Euler angles: φ, θ, and ψ are used to specify any particular orientation according to the *Z*–*Y*–*Z* Euler angle rotation convention (Fig. 1a). These rotations permit a simple expression for the projected area of an ellipsoid (cf. Vickers 1996):

$$\begin{aligned} A_{\text{proj}} &= \pi \sqrt{a^2 b^2 \cos^2\psi \sin^2\theta + a^2 c^2 \sin^2\psi \sin^2\theta + b^2 c^2 \cos^2\theta} \\ &= \pi a^2 \sqrt{\varphi_{ba}^2 \cos^2\psi \sin^2\theta + \varphi_{ca}^2 \sin^2\psi \sin^2\theta + \varphi_{ba}^2 \varphi_{ca}^2 \cos^2\theta} \\ &= \pi a^2 \Psi_{\text{proj}}, \end{aligned} \tag{6}$$

where $a \geq b \geq c$. Notice that only the last two Euler angles θ and ψ change the projected area whereas the first rotation φ changes the angle of the projected ellipse maximum dimension from the x axis. The minimum value of Ψ_{proj} is $\varphi_{ba}\varphi_{ca}$ ($\theta = 0°$ and $\psi = \psi$; as shown in Fig. 1c) whereas the maximum

value is φ_{ba} ($\theta = 90°$ and $\psi = 0°$; as shown in Fig. 1d). It is often thought that $\Psi_{\text{proj}} \approx \varphi_{ba}$ (e.g., Magono and Nakamura 1965; Szyrmer and Zawadzki 2010), yet the correct distribution of orientations is still largely uncertain. The projected area geometric factor Ψ_{proj} can be approximated as power-law combinations of φ_{ba} and φ_{ca}:

$$\Psi_{\text{proj}} \approx \langle \Psi_{\text{proj}} \rangle \approx \varphi_{ba}^{\Psi_{ba}} \varphi_{ca}^{\Psi_{ca}}, \tag{7}$$

where Ψ_{ba} and Ψ_{ca} are exponents that represent the contribution of each ellipsoid aspect ratio toward the average projection for an assumed orientation distribution and brackets represent an orientation average. A power-law fit for random orientations is given by $\Psi_{ba} = 0.9$ and $\Psi_{ca} = 0.5$. Figure 2 shows that the absolute error between the power-law approximation and a Monte Carlo estimate of the actual average quantity for $\langle \Psi_{\text{proj}} \rangle$ is very close to zero right where the MASC bivariate beta distribution reaches a peak. Throughout this paper, $A_{\text{proj}} \approx \langle A_{\text{proj}} \rangle$ so that Eq. (7) can be used with Eq. (4) to incorporate the effects of random and horizontal orientations into fall speed and self-aggregation calculations.

Calculating N_{Re} for triaxial ellipsoids is based on the analytical power-law approach of Khvorostyanov and Curry (2005), where

$$N_{\text{Re}} = \overline{a}_m X^{\overline{b}_m}, \tag{8}$$

and the coefficients $\overline{a}_m$ and $\overline{b}_m$ are determined using the method of Khvorostyanov and Curry (2002), Mitchell and Heymsfield (2005), Khvorostyanov and Curry (2005), and Heymsfield and Westbrook (2010) for the number-weighted mean Best number $\overline{X}$. The use of a number-weighted Best number to diagnose $\overline{a}_m$ and $\overline{b}_m$ is somewhat arbitrary; other bulk weightings (e.g., mass or area) of X could also be used since the ratio of mass to projected area is the critical parameter that determines the overall behavior of the Best number. Despite these more involved bulk weightings, the tests in this study instead use the number-weighted Best number so as to be consistent with a newer microphysics scheme: the Ice-Spheroids Habit Model with Aspect-Ratio Evolution (ISHMAEL; Jensen et al. 2017). This average Best number approximation can then be used to develop a general form for all drag parameterization schemes:

$$\overline{b}_m = \frac{C_1\sqrt{\overline{X}}}{2\left(\sqrt{1+C_1\sqrt{\overline{X}}}-1\right)\sqrt{1+C_1\sqrt{\overline{X}}}} - \frac{a_o b_o \overline{X}^{b_o}}{C_2\left(\sqrt{1+C_1\sqrt{\overline{X}}}-1\right)^2} - \Delta_t, \tag{9a}$$

$$\overline{a}_m = \overline{\psi}_t \frac{C_2\left(\sqrt{1+C_1\sqrt{\overline{X}}}-1\right)^2 - a_o \overline{X}^{b_o}}{\overline{X}^{\overline{b}_m}}, \tag{9b}$$

where $C_2 = \delta_0^2/4$ and $C_1 = (C_o C_2)^{-1/2}$. For the approach of Mitchell and Heymsfield (2005), $a_o = 1.7 \times 10^{-3}$ and $b_o = 0.8$ represents a turbulence correction whereas $a_o = b_o = 0$ for all other approaches. For Heymsfield and Westbrook (2010), $C_o = 0.35$ and $\delta_0 = 0.8$ whereas all other schemes have $C_o = 0.6$ and $\delta_0 = 5.83$; Δ_t and $\overline{\psi}_t$ are turbulence correction terms for the approach of Khvorostyanov and Curry (2005) that can be found in their paper. For all other methods, $\Delta_t = 0$ and $\overline{\psi}_t = 1$. Figure 3 shows how these different parameterization schemes influence the resulting fall speed parameters for assumed reduced-density sphere/fractal aggregates. The majority of the differences between these various schemes occurs at larger sizes where turbulence is expected to increase drag. These drag parameterization schemes are used in section 3 to thoroughly test the sensitivity of the proposed ellipsoid methodology compared to the traditional sphere (fractal) approach of previous studies.

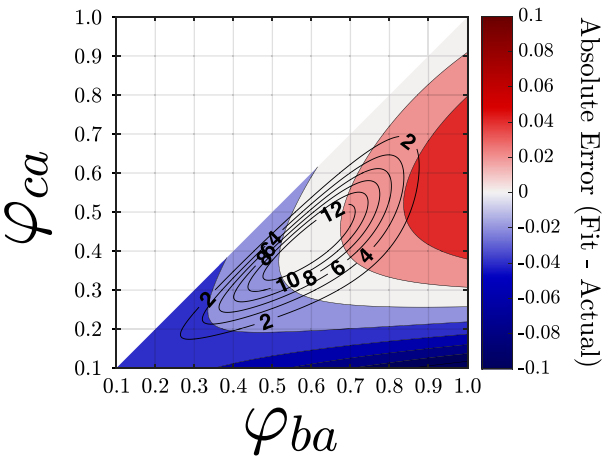

FIG. 2. (filled) Absolute error in $\langle \Psi_{\text{proj}} \rangle$ between power-law parameterization (fit) where $\Psi_{ba} = 0.9$ and $\Psi_{ca} = 0.5$ and the Monte Carlo estimate (actual). Black contours show the bivariate beta probability distribution function [Eq. (2)] given in increments of 2.

The Best number can be represented in a general form (cf. Böhm 1989; Heymsfield and Westbrook 2010):

$$X = \frac{8mg\rho_a}{\pi\eta_a^2} A_r|_{\text{ellip}}^{-k_c} = \frac{8mg\rho_a}{\pi\eta_a^2} A_r|_{\text{sph}}^{-k_c} \varphi_{ba}^{k_c\Psi_{ba}} \varphi_{ca}^{k_c\Psi_{ca}}, \tag{10}$$

where $A_r|_{\text{ellip}}$ is the ellipse area ratio representing the projected particle area, A_{part}, to the ellipsoid projected area, A_{proj} and $A_r|_{\text{sph}}$ is the analogous area ratio quantity for spheres[1] (see Fig. 1b). Notice that the form of Eq. (10) is the same as the semiempirical relationship inferred by Heymsfield and Westbrook (2010) but

[1] Often derived from in situ observations in terms of the maximum *projected* span L rather than the maximum *particle* dimension D with the assumption that $L \approx D$. This provides an obvious inconsistency in Fig. 1b, where $A_{\text{circ}} \neq (\pi/4)L^2$. For simplicity, this inconsistency is ignored in Fig. 1 in order to maintain the mathematical relationship between $A_r|_{\text{ellip}}$ and $A_r|_{\text{sph}}$ based on the size and shape of the aggregate itself rather than its projection.

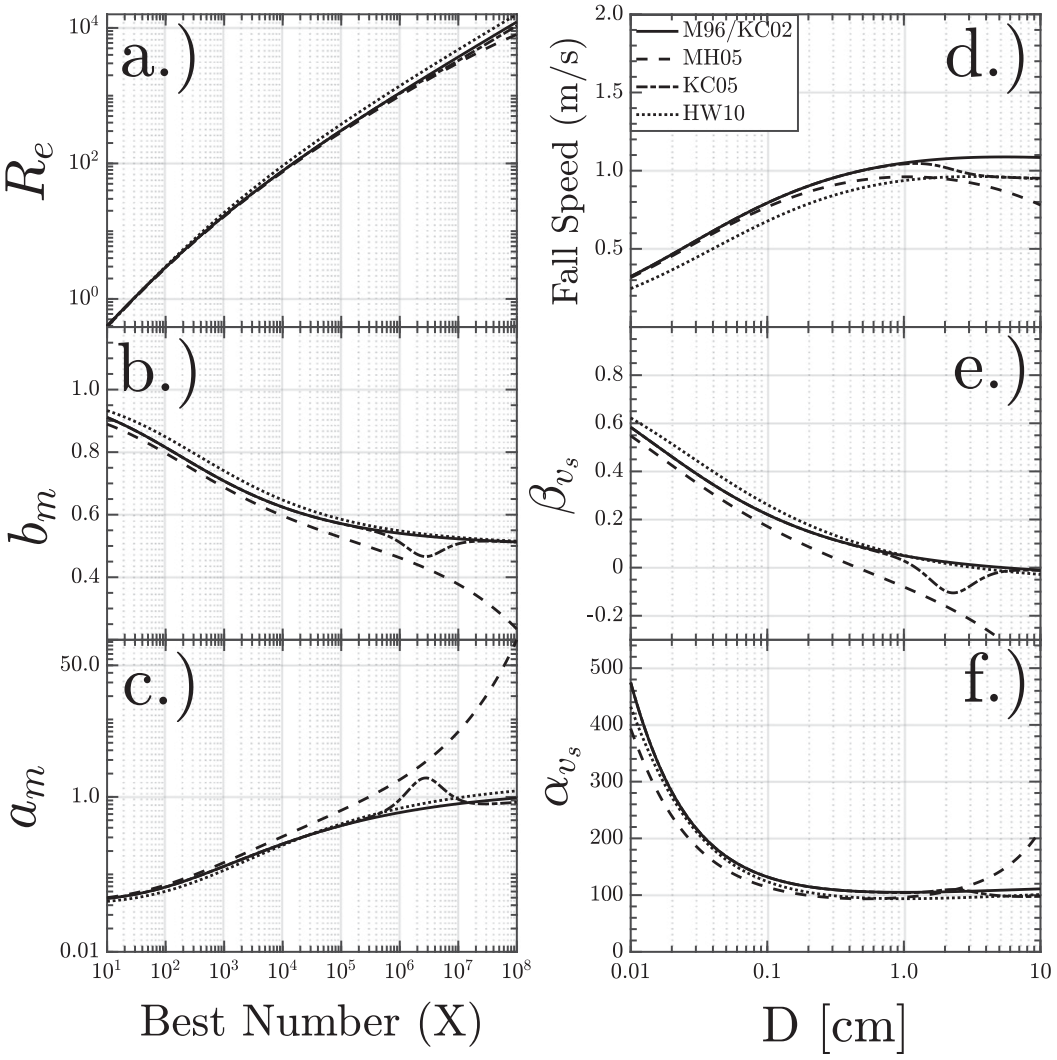

FIG. 3. Comparison of aggregate fall speed properties following Mitchell [1996 (M96); solid], Khvorostyanov and Curry [2002 (KC02); solid], Mitchell and Heymsfield [2005 (MH05); dashed], Heymsfield and Westbrook [2010 (HW10); dotted], and Khvorostyanov and Curry [2005 (KC05); dash–dotted]. Subplots show (a) X vs R_e, (b) X vs b_m, (c) X vs a_m, (d) D vs v_t, (e) D vs β_{v_s}, and (f) D vs α_{v_s}. D represents the maximum aggregate dimension whereas α_{v_s} and β_{v_s} are the spherical/fractal aggregate v_t–D power-law prefactor and exponent, respectively.

with $A_r|_{\text{ellip}}$ instead of $A_r|_{\text{sph}}$ where $k_c = 1$ for the approaches of Mitchell (1996), Mitchell and Heymsfield (2005), and Khvorostyanov and Curry (2005), $k_c = 0.5$ for the approach of Heymsfield and Westbrook (2010), and $k_c = 0.25$ for the oblate spheroid approach of Böhm (1989, 1992). For the current paper, it is not clear which of these exponents would be most appropriate. Therefore, this study uses $k_c = 1.0$ for the approaches of Mitchell (1996), Mitchell and Heymsfield (2005), and Khvorostyanov and Curry (2005) and $k_c = 0.5$ for the approach of Heymsfield and Westbrook (2010). The approximation of Böhm (1989, 1992) where $k_c = 0.25$ is not appropriate for assumed triaxial ellipsoids because the vast majority of these ellipsoids are not oblate (see Jiang et al. 2019; Dunnavan et al. 2019).

The area ratio can be determined by combining Eq. (6) and the A_{part} parameterization provided in Table 1 of Mitchell (1996):

$$A_{\text{part}} = \sigma D^{\varsigma} = 2^{\varsigma}\sigma a^{\varsigma}, \tag{11}$$

where this study uses the parameterization from Mitchell (1996) where $\sigma = 0.2285$ and $\varsigma = 1.88$ (cgs units). Other parameterizations exist for the projected particle area for aggregates (cf. Heymsfield and Miloshevich 2003). However, as pointed out by Heymsfield and Miloshevich (2003), these different parameterizations are rather close in value to ones from Mitchell (1996). Therefore, the tests in this study use only this set of values. Dividing Eq. (11) by Eq. (6) gives the ellipse area ratio

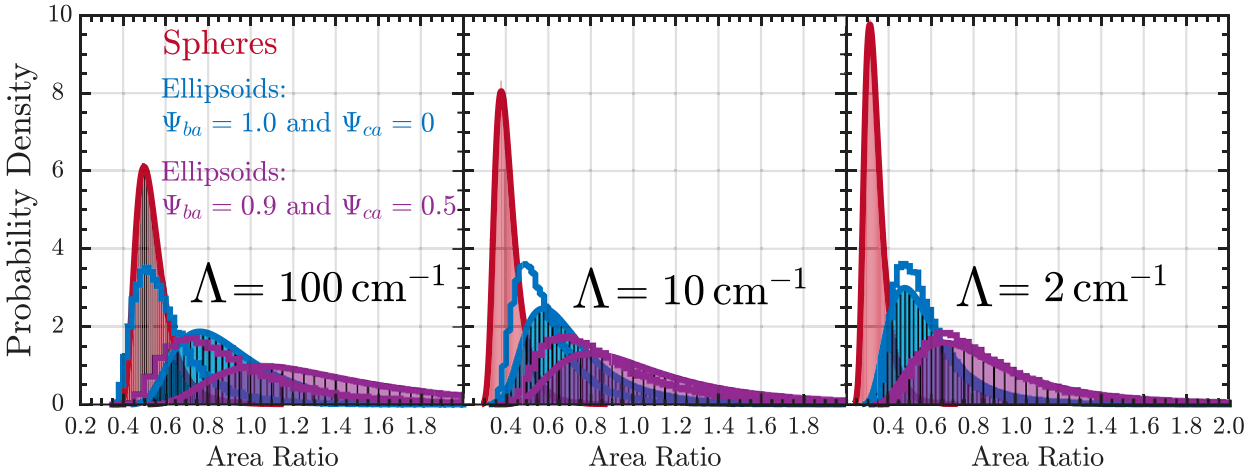

FIG. 4. Probability distributions of $A_r|_{\mathrm{sph}}$ and $A_r|_{\mathrm{ellip}}$ for (left) $\Lambda = 100\,\mathrm{cm}^{-1}$, (center) $\Lambda = 10\,\mathrm{cm}^{-1}$, and (right) $\Lambda = 2.0\,\mathrm{cm}^{-1}$. Shaded histograms represents the distributions computed by sampling from each discretized distribution whereas solid lines correspond to the distributions computed from the analytical H-function representation given in the supplementary materials section. Staircases for the ellipsoid computations correspond to distributions with maximum dimensions that are in between the cloud probe limits used by Heymsfield et al. (2002a). Ellipsoid distributions represent area ratios for horizontally oriented (blue) and randomly oriented aggregates (purple) with power-law parameterizations given in the text.

$$A_r|_{\mathrm{ellip}} = \frac{A_{\mathrm{part}}}{A_{\mathrm{proj}}} = A_r|_{\mathrm{sph}} \varphi_{ba}^{-\Psi_{ba}} \varphi_{ca}^{-\Psi_{ca}} = \frac{2^s}{\pi} a^{s-2} \varphi_{ba}^{-\Psi_{ba}} \varphi_{ca}^{-\Psi_{ca}}$$

$$= \alpha_{AR} a^{\beta_{AR}} \varphi_{ba}^{-\Psi_{ba}} \varphi_{ca}^{-\Psi_{ca}}, \tag{12}$$

where $A_r|_{\mathrm{sph}} = A_{\mathrm{part}}/(\pi a^2)$ (see Fig. 1b).

Figure 4 shows the area ratio distributions that result from the above parameterization method for different values of Λ. The $A_r|_{\mathrm{sph}}$ distribution becomes more sharply peaked and has its mode shifted to smaller values for smaller Λ. The additional aspect ratio factors in the formulation of $A_r|_{\mathrm{ellip}}$ act to spread out the $A_r|_{\mathrm{sph}}$ distribution to larger area ratios. Horizontally and randomly oriented ellipsoids both have nonzero probability for $A_r|_{\mathrm{ellip}} > 1.0$. This is the result of using the above inverse procedure to specify area ratio whereby ellipsoid shapes and orientations necessarily increase area ratios. It is important to note that these large area ratio values can be considered unphysical according to the interpretation of Böhm (1989). This issue with unphysical area ratio values becomes more pronounced when ellipsoids are randomly oriented because horizontal orientations maximize A_{proj}. These unphysical values result from using the in situ derived parameters of Mitchell (1996) which are strictly appropriate only for a truncated range of projected maximum dimensions that are consistent within probe limits. Using this same truncated range for ellipsoid projected areas results in a more realistic distribution, at least for horizontally oriented ellipsoids. Throughout this study, the full area ratio distributions will be used when characterizing fall speed. Although the unrealistic area ratio values provide a limitation for this study, the use of these area ratios will provide a set of sensitivity tests for shape and orientation in the resulting calculations.

The effective aggregate sphere density is assumed to follow the empirical hybrid parameterization given by Table 1 of Heymsfield et al. (2002a):

$$\rho_s(a) = 2^{\alpha} k A_r^n|_{\mathrm{sph}} a^{\alpha}$$

$$= \alpha_{\rho_s} a^{\beta_{\rho_s}}, \tag{13}$$

where k, n, and α are parameters developed from in situ datasets such as Heymsfield et al. (2002a) and α_{ρ_s} and β_{ρ_s} are given in the appendix. In this study, $n = 1.5$ which is consistent with all parameterizations. Additionally, three sets of k and α are used to test the sensitivity of fall speed and self-aggregation to various M–D exponents of spherical aggregates (β_{m_s}). These values are from Heymsfield et al. (2002a) where $k = 0.015$ and $\alpha = -1$ ($\beta_{m_s} \approx 1.8$) and from Heymsfield et al. (2002b) where $k = 0.054$ and $\alpha = -0.8$ ($\beta_{m_s} \approx 2.0$), and $k = 0.078$ and $\alpha = -0.6$ ($\beta_{m_s} \approx 2.2$). All values are given in terms of cgs units. With this parameterization, the aggregate mass for spheres can be expressed as

$$m = \alpha_{m_s} a^{\beta_{m_s}}. \tag{14}$$

Values of α_{m_s} range from 0.000 544 to 0.004 03 $\mathrm{g\,cm}^{-\beta_{m_s}}$ which yield mean aggregate mass values $\overline{m} = q_i/N_i$ that range from 3.85×10^{-5} to 13.6 mg for $\Lambda = 100\,\mathrm{cm}^{-1}$ to $\Lambda = 2\,\mathrm{cm}^{-1}$, respectively. This hybrid approach therefore corresponds to a wide variety of rimed and unrimed aggregates (cf. Locatelli and Hobbs 1974; Kajikawa and Heymsfield 1989; Mitchell 1996; Heymsfield et al. 2002a,b; Field and Heymsfield 2003; Schmitt and Heymsfield 2010) and are not necessarily representative of any particular type. The mass of an ellipsoidal aggregate is given as

$$m = \frac{4}{3} \pi \rho_e a^3 \varphi_{ba} \varphi_{ca}. \tag{15}$$

The variable ρ_e here refers to the effective ellipsoid density of the aggregates. If ellipsoidal aggregates exhibit the same spherical effective density as Eq. (13), then

$$m = \frac{4}{3}\pi[\rho_s \times (\varphi_{ba}\varphi_{ca})^{-1}]a^{3+\beta_{\rho_s}}\varphi_{ba}\varphi_{ca}$$
$$= \frac{4}{3}\pi\alpha_{\rho_s}a^{3+\beta_{\rho_s}}$$
$$= \alpha_{m_s}a^{\beta_{m_s}}. \quad (16)$$

This implies that using the typical constraint of a spherical effective density negates the influence of aspect ratio dispersion on mass. In this case, the mass distribution is the same for ellipsoids as for spheres. Tests using this assumption can therefore be thought of as a microphysical *model* constraint in absence of an assumed ellipsoid effective density parameterization. Alternatively, ellipsoidal aggregates can also exhibit a similar power-law like relation with size such that

$$m = \frac{4}{3}\pi\alpha_{\rho_e}a^{3+\beta_{\rho_e}}\varphi_{ba}\varphi_{ca}$$
$$= \alpha_m a^{\beta_m}\varphi_{ba}\varphi_{ca}, \quad (17)$$

where α_{ρ_e} and β_{ρ_e} are effective ellipsoid density parameters. For consistency, both assumptions are used in the sensitivity tests presented in section 3. Tests with the same *M–D* relationships between typical power-law relations and for ellipsoidal particles use Eq. (16). This assumption would be consistent for bulk microphysics models where bulk quantities like IWC or reflectivity are predicted. Tests using Eq. (17) on the other hand maintain a shape-induced mass dispersion. Unfortunately, there are not many datasets of projected ellipse area ratios that could be used to infer the parameters in ρ_e. In addition, the 3D asymmetry of triaxial ellipsoids makes such a parameterization rather involved if projected aspect ratios are used to inform ρ_e. Instead, this study fixes the first two mass moments of both the spherical and ellipsoid distributions so as to diagnose α_{ρ_e} and β_{ρ_e}. Such a constraint is especially useful because observational estimates of both IWC and reflectivity are assumed proportional to the first and second mass distribution moments of the particle distribution function. Therefore, using the same two moments between the spherical and ellipsoidal cases necessarily constrains both cases as identical from an *observational* standpoint.

The Best number can now be expressed using Eqs. (10), (12), and (15):

$$X = \alpha_X a^{\beta_X}\varphi_{ba}^{\chi_{ba}}\varphi_{ca}^{\chi_{ca}}, \quad (18)$$

where $\chi_{ba} = k_c\Psi_{ba}$ and $\chi_{ca} = k_c\Psi_{ca}$ if Eq. (14) is used and $\chi_{ba} = k_c\Psi_{ba} + 1$ and $\chi_{ca} = k_c\Psi_{ca} + 1$ if Eq. (15) is used. α_X and β_X are the Best number power-law parameters given in the appendix. Combining Eqs. (5), (12), (15), and (18) yields

$$v_t = \frac{1}{2}\frac{\eta_a}{\rho_a}\overline{a}_m\alpha_X^{\frac{\overline{b}_m}{\beta_X\overline{b}_m - 1}}\varphi_{ba}^{\chi_{ba}\overline{b}_m - \psi_{ba}/2}\varphi_{ca}^{\chi_{ca}\overline{b}_m - \psi_{ca}/2}$$
$$= \alpha_v a^{\beta_v}\varphi_{ba}^{v_{ba}}\varphi_{ca}^{v_{ca}}. \quad (19)$$

c. Self-aggregation

The equations for mass, projected area, and fall speed given in the previous section can be used to calculate aggregation self-aggregation rates. The governing equation for collection (aggregation) is called the stochastic collection equation (SCE) which is given by

$$\frac{\partial n(x,t)}{dt} = \frac{1}{2}\int_{y=0}^{x} K(x-y,y)n(x-y,t)n(y,t)\,dy - \int_{y=0}^{\infty} K(x,y)n(x,t)n(y,t)\,dy, \quad (20)$$

where x and y are masses of two aggregating particles, $K(x, y)$ is the collection kernel which describes the physics of the aggregation process, and $n(x, t)$ is the number distribution function for all particles at time t. It is common to write Eq. (20) in terms of distribution moments by integrating both sides of Eq. (20) [i.e., $\int_{x=0}^{\infty}x^r f(x, t)\,dx$]. A transformation of this new equation (see Bleck 1970) gives

$$\frac{dM_r}{dt} = \frac{1}{2}\int_{x=0}^{\infty}\int_{y=0}^{\infty}[(x+y)^r - x^r - y^r]K(x,y)n(x,t)n(y,t)\,dx\,dy, \quad (21)$$

where M_r denotes the value of the rth moment of the number distribution function (for more details, see Thompson 1968). Throughout this study, the number distribution function is represented in terms of mass such that the zeroth, first, and second moments can be considered proportional to total number, mass, and reflectivity (assuming Rayleigh scattering), respectively. By convention, the first moment does not change (i.e., mass is conserved during aggregation). However, the zeroth and second moments can be expressed in terms of the simplified form[2]

$$\frac{dM_r}{dt} = (-1)^{p+1}\frac{p+1}{2}\int_{x=0}^{\infty}\int_{y=0}^{\infty}x^p y^q K(x,y)n(x,t)n(y,t)\,dx\,dy, \quad (22)$$

when $r = 0 (p = q = 0)$ and $r = 2 (p = q = 1)$. Partial moments such as the conversion of mass from one category to another (i.e., Verlinde et al. 1990) can be expressed for $r = 1$ when $p = 1$ and $q = 0$. For self-aggregation, $q = p$.

Typically, the collection kernel for aggregation $K(x, y)$ is represented in terms of a hydrodynamic kernel given by (cf. Connolly et al. 2012)

$$K(x,y) = E_{\text{agg}}\left|v_{t_x} - v_{t_y}\right|\left(\sqrt{A_{\text{proj},x}} + \sqrt{A_{\text{proj},y}}\right)^2, \quad (23)$$

where the subscripts x and y represent each collecting species and E_{agg} represents the aggregation efficiency. It is often the case that the fall speed term in Eq. (23) complicates evaluation of Eq. (22) because of the discontinuity provided by the absolute value function. This has led to the use of either analytical approximations (Wisner et al. 1972; Seifert et al. 2014) or computationally expensive general solutions (Passarelli 1978;

[2] Note: This form is only appropriate for $r = 0$ and $r = 2$. Other integer moments can also simplify by using a binomial coefficient expansion. See Drake (1972) for details.

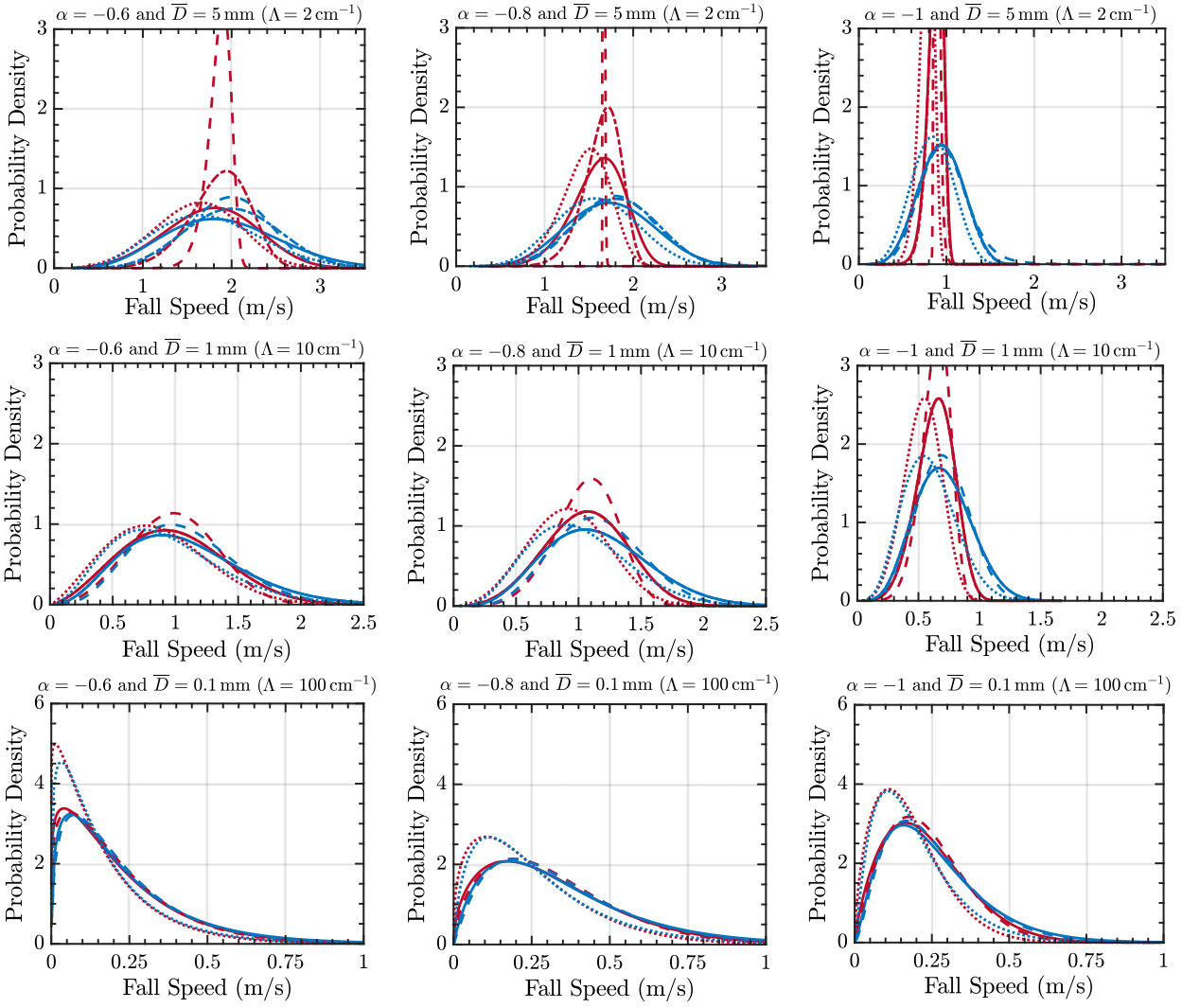

FIG. 5. Comparison between spheres and a bivariate distribution of ellipsoids when calculating fall speed for different drag parameterization methods, α values, and Λ values. Red lines correspond to calculations assuming spheres whereas blue lines represent calculations using ellipsoids. Line style denotes the chosen fall speed parameterization following Mitchell (1996), Khvorostyanov and Curry (2002) (solid), Mitchell and Heymsfield (2005) (dashed), Heymsfield and Westbrook (2010) (dotted), and Khvorostyanov and Curry (2005) (dash–dotted). Notice that the axis limits are different for various panels to highlight changes in the fall speed distribution.

Verlinde et al. 1990) expressed in terms of hypergeometric functions.

Normally, Eq. (22) is a double integral. However, the use of the bivariate beta distribution for ellipsoidal shape complicates the evaluation of this integral by increasing the dimensionality to six for self-aggregation. It is simple to analytically integrate Eq. (22) using any of the fall speed difference approximations for bivariate beta distributed ellipsoid aspect ratios. However, the use of the full hydrodynamic kernel becomes quite complicated due to the size and shape influence on the integral limits when splitting the absolute value function into two terms (cf. Verlinde et al. 1990). Therefore, the self-aggregation rates in this study are estimated using a Monte Carlo approach for evaluating Eq. (22) with Eq. (23) where the gamma and bivariate beta distributions are discretized and sampled 10 000 times. Each sampled set of m, v_t, and A_{proj} then is used to estimate the integrated collection kernel for number and reflectivity. For simplicity, E_{agg} and N_i are both normalized to unity.

For all tests, $2 \leq \Lambda \leq 100\,\text{cm}^{-1}$. This range is consistent with the observations from Heymsfield et al. (2002a) and Lawson et al. (1998) although the lower end of Λ is almost always closer to $10\,\text{cm}^{-1}$ rather than $2\,\text{cm}^{-1}$ (Lo and Passarelli 1982; Mitchell 1988). Many studies (e.g., Heymsfield et al. 2002a) show that Λ values of $2\,\text{cm}^{-1}$ or below are unlikely. Therefore, the sensitivity test results in the next section should be viewed as encompassing the beginning stages of aggregation ($\Lambda \sim 100\,\text{cm}^{-1}$), late stages of aggregation ($\Lambda \sim 10\,\text{cm}^{-1}$), and the rare case of

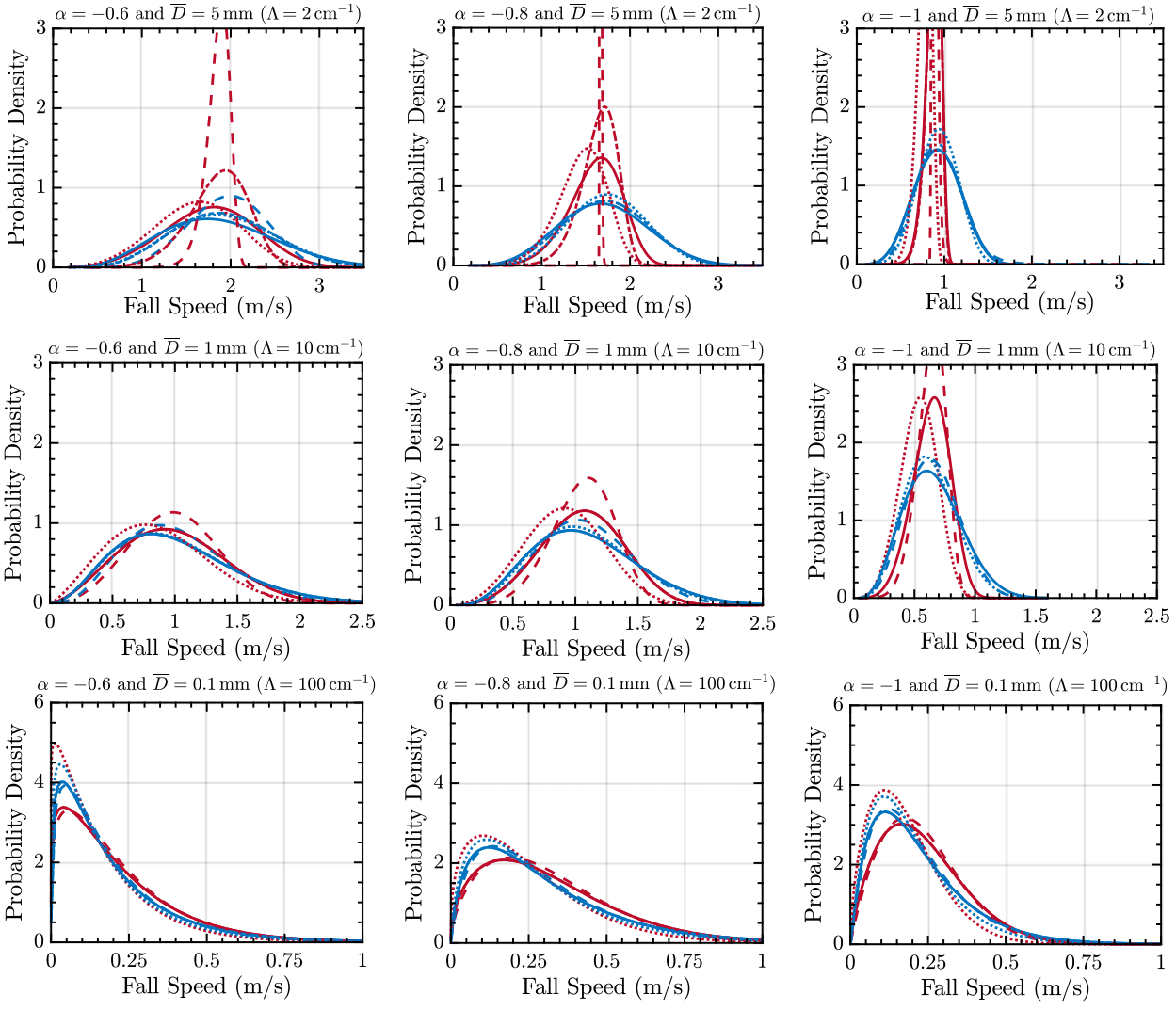

FIG. 6. As in Fig. 5, but with ellipsoids that exhibit the same area ratio as spheres.

extremely large aggregates ($\Lambda \sim 2\,\mathrm{cm}^{-1}$; e.g., Lawson et al. 1998). This last case is specifically designed to investigate how aggregate shapes and orientations are expected to impact the limiting behavior of the fall speed distribution and self-aggregation rates in the absence of secondary ice production processes such as collisional breakup.

3. Results

a. *Fall speed*

1) AGGREGATE SHAPE EFFECT

Figure 5 compares the fall speed distributions (see supplementary materials) between the traditional power-law approaches when assuming spheres (fractals) and when assuming ellipsoids with aspect ratios governed by Eq. (2) for different slope parameters (Λ) and β_{m_s} [as dictated by the α exponent in Eq. (13), the area ratio-density parameterization]. For this series of subplots, *both* mass and projected area exhibit dispersion for the same maximum dimension and aggregates are assumed to fall such that their projected areas maximize (i.e., $\Psi_{ba} = 1.0$ and $\Psi_{ca} = 0$). For large slope parameters (small mean maximum dimensions), the introduction of shape dispersion does not significantly alter the fall speed distribution. However, smaller values of Λ (i.e., $\Lambda = 10\,\mathrm{cm}^{-1}$ and $\Lambda = 2\,\mathrm{cm}^{-1}$) lead to a narrowing of the sphere fall speed distribution which become more pronounced when the density exponent α equals -1. Importantly, *ellipsoids do not narrow regardless of slope parameter*. In fact, aggregate shapes appear to *spread out* the fall speed distribution as Λ decreases. The increased ellipsoid fall speed dispersion consequently extends the tail of the fall speed distribution more than spheres. This extended tail suggests that bulk quantities which depend upon fall speed, such as mass-weighted fall speed, are perhaps underestimated when assuming spherical or fractal aggregates. For very small values of $\Lambda = 2.0\,\mathrm{cm}^{-1}$, the fall speed distribution for spheres

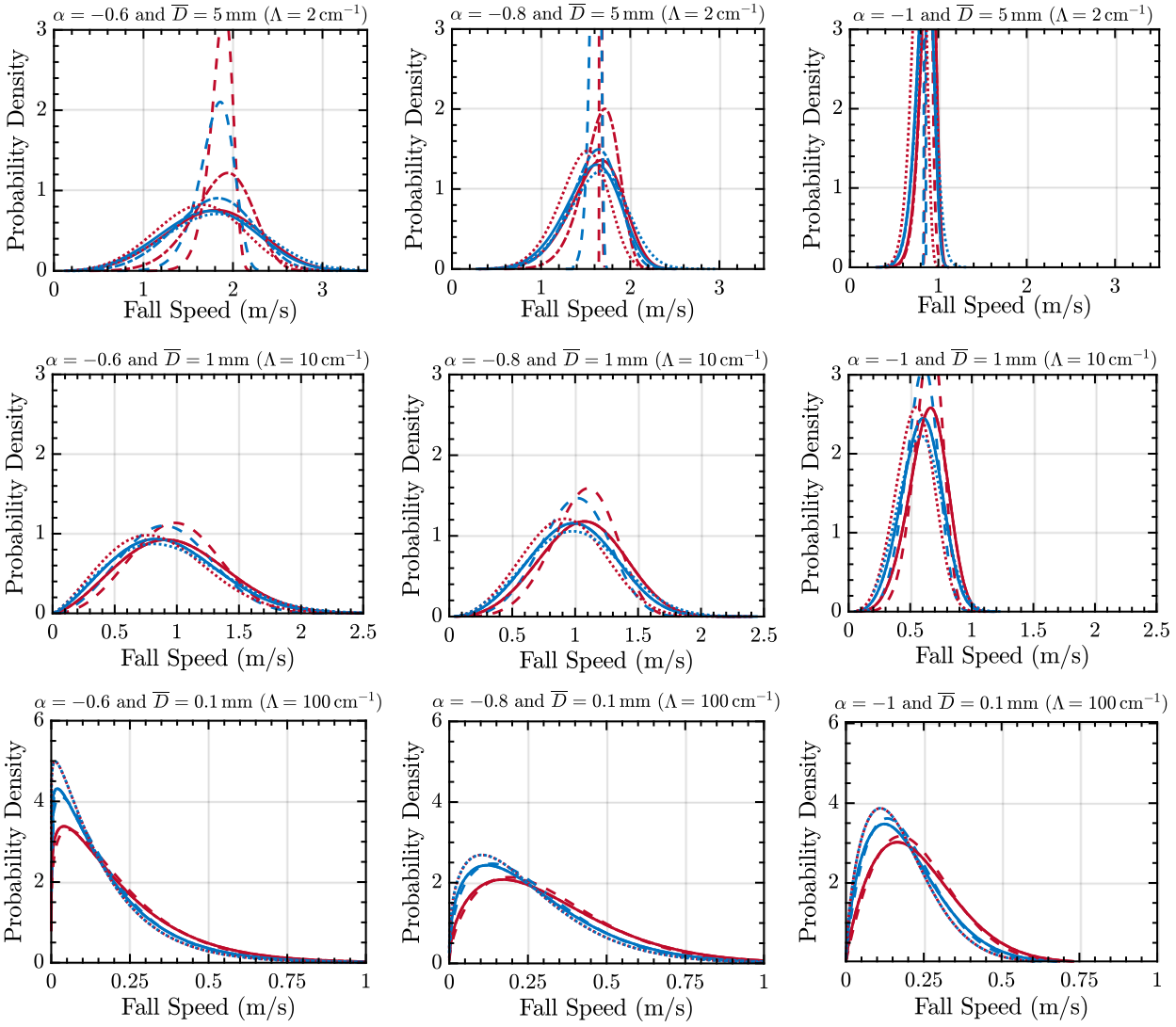

FIG. 7. As in Fig. 5, but with ellipsoids that exhibit the same mass distribution as spheres.

becomes very narrow whereas ellipsoids maintain a disperse fall speed distribution regardless of $\alpha(\beta_{m_s})$.

Because aggregate shapes impact both mass and projected area, it is not initially clear which component contributes to the consistent disperse nature of $n(v_t)$ for ellipsoids. To investigate the underlying cause, Fig. 5 was reproduced with the exception that the same area ratio or the same mass distribution was used for both spheres and ellipsoids. When controlling for area ratio (Fig. 6), the distributions for ellipsoids appear visually similar to that in Fig. 5. The primary difference between both figures is that Fig. 6 for ellipsoids has its mode shifted more toward smaller fall speeds. Besides this change, both distributions are visually identical. When controlling for mass (Fig. 7), the ellipsoid distribution appears closer to that of spheres. As in Fig. 6, large values of Λ for ellipsoids lead to a fall speed peak at smaller values compared to spheres. However, small values of Λ in Fig. 7 lead to a pronounced narrowing of the fall speed distribution for ellipsoids. Therefore, it is clear that the major contribution of shape dispersion on fall speed comes from the *increased dispersion of aggregate mass at a particular size* rather than a *decrease in projected area*.

The effects of aggregate shape on bulk fall speed quantities (number-, mass-, and reflectivity-weighted fall speeds) can be seen in Fig. 8 for ellipsoids that exhibit shape-induced mass and projected area dispersions for the same maximum dimension. In general, ellipsoids exhibit larger mean fall speeds than spheres where the difference between spheres and ellipsoids becomes larger for smaller values of α (larger values of β_m) and for higher-ordered mass fall speed moments (i.e., mass-weighted and reflectivity-weighted fall speed). The largest differences between spheres and ellipsoids also occur at higher values of Λ and become closer to one another for smaller values of Λ. Smaller values of Λ act to decrease results using Mitchell and Heymsfield (2005) as compared to the other drag parameterizations. Much of the

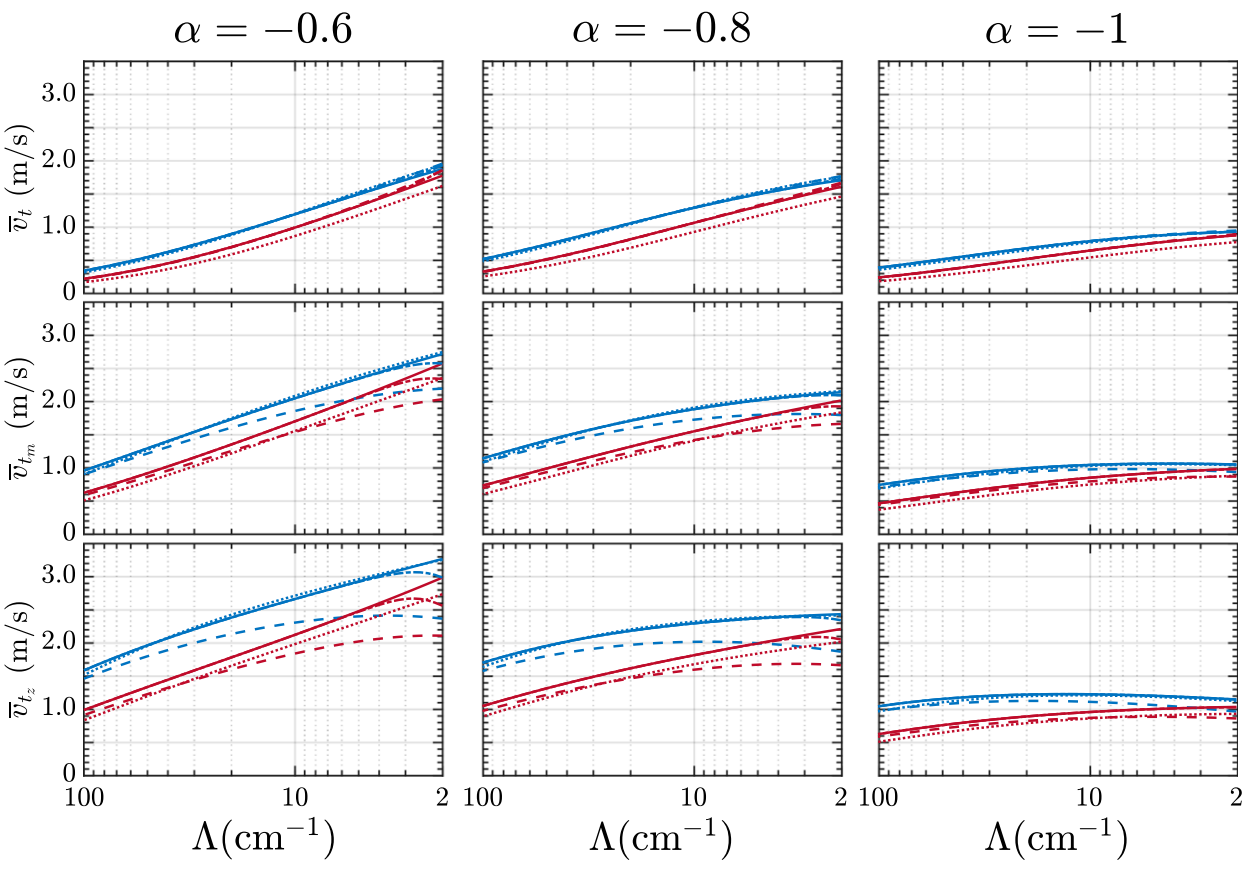

FIG. 8. Comparison of (top) number-weighted, (middle) mass-weighted, and (bottom) reflectivity-weighted distribution mean fall speeds as a function of slope parameter Λ for different values of α. Ellipsoids of the same size exhibit shape-induced dispersion of both mass and projected area.

influence of α on number-weighted fall speed quantities exists between $\alpha = -1$ ($\beta_{m_s} \approx 1.8$) and $\alpha = -0.8$ ($\beta_{m_s} \approx 2.0$) for both spheres and ellipsoids. However, mass- and reflectivity-weighted fall speed are strongly affected by decreases in α even for various drag parameterization schemes. As stated before, the extended tail of the fall speed distribution for ellipsoids leads to their higher mean fall speed values. Overall, Fig. 8 shows that high mass and fall speed moments can increase by almost 60% due to shape and orientation alone.

2) ORIENTATION EFFECTS

Figure 9 compares the horizontally oriented mean ellipsoid bulk fall speed quantities from Fig. 8 to randomly oriented ellipsoids. The change in orientation produces about 10% difference where the largest differences occur at larger Λ for all drag parameterization schemes except for Heymsfield and Westbrook (2010) which has $k_c = 0.5$. For the other drag parameterizations, randomly oriented ellipsoids have smaller mean fall speeds than horizontally oriented ellipsoids. Higher-order fall speed quantities yield smaller differences between horizontally and randomly oriented ellipsoids. This can be explained by how mass impacts the fall speed more than projected area as illustrated in Figs. 5 and 6. Therefore, orientations produce a relatively mild effect on fall speed even when considering the unphysical behavior of the ellipsoidal area ratio distribution produced by the Mitchell (1996) particle area parameterization.

b. *Self-aggregation*

1) AGGREGATE SHAPE EFFECT

Figure 10 shows the absolute value of self-aggregation rates for number and reflectivity for the distributions from Figs. 5 and 8. Self-aggregation rates generally increase as a power-law with decreasing Λ where the horizontally oriented ellipsoids yield smaller self-aggregation rates than spheres of the same size. This, in general, results from ellipsoids exhibiting a smaller projected area in Eq. (23) than spheres. Ellipsoids therefore produce two competing self-aggregation effects. As shown in Fig. 5, the introduction of ellipsoid shape dispersion for a given size acts to increase the fall speed distribution standard deviation which, in turn, increases the fall speed term in Eq. (23). At the same time, however, the use of ellipsoids acts to decrease the projected area for aggregates of a particular size which directly decreases the area term in Eq. (23). Despite the nonlinearities due to shape and orientation, self-aggregation rates for the majority of Λ values are rather similar between spheres and ellipsoids where ellipsoids exhibit slightly larger self-aggregation

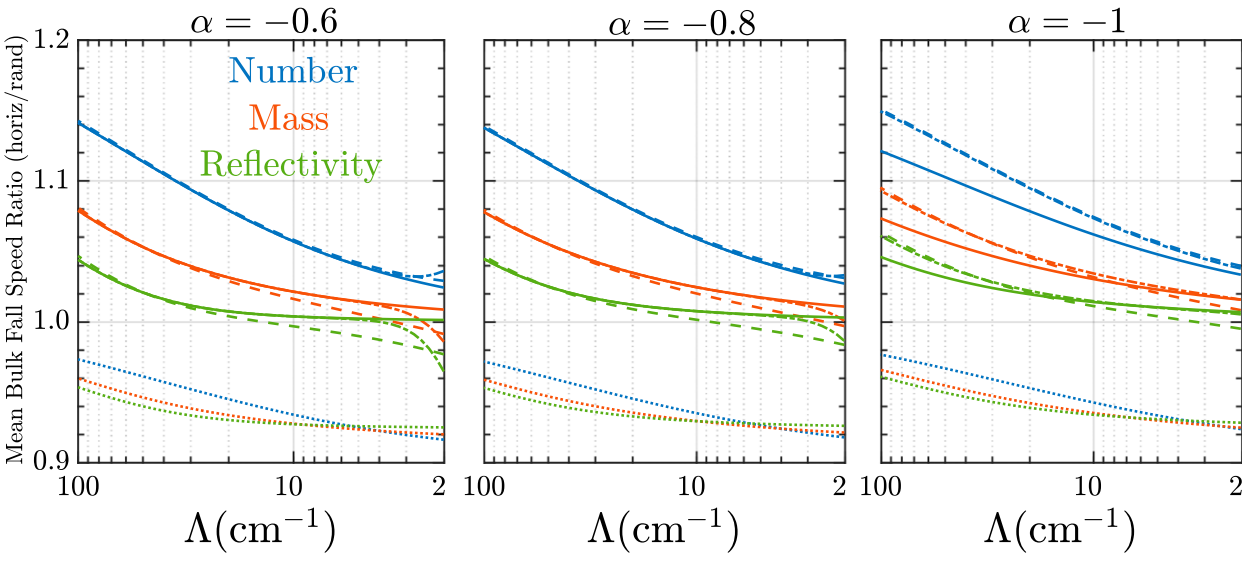

FIG. 9. As in Fig. 8, but for the ratio of bulk fall speeds between horizontally oriented and randomly oriented aggregates. Various colors reflect different bulk fall speed quantities: number-, mass-, and reflectivity-weighted fall speed for a given α and drag parameterization scheme.

rates for small values of Λ. An important exception is when the drag parameterization of Mitchell and Heymsfield (2005) is employed. For this drag scheme, sphere self-aggregation rates drop precipitously as Λ approaches 2 cm^{-1}. This sharp transition occurs because of the rapid narrowing of the fall speed distribution when $\beta_{v_s} \to 0$ (Fig. 5). As a result, the ratio of ellipsoid to sphere number and reflectivity self-aggregation explodes to a factor greater than 100. The value of α affects self-aggregation rates primarily for small Λ such that ellipsoids yield smaller self-aggregation rates than spheres when $\alpha = -0.6$ but greater rates for ellipsoids when $\alpha = -1$. Greater values of $\alpha(\beta_m)$ therefore yield consistently smaller self-aggregation rates than spheres where the ratio is approximately 0.6 for number.

The same fall speed sensitivity tests were also conducted for self-aggregation. This can be seen in Figs. 11 and 12 which represent a comparison of rates between ellipsoidal and sphere aggregates with the same area ratio and the same mass distribution, respectively. Like Fig. 6, ellipsoids with the same area ratio as spheres yield results that are visually similar to ellipsoids where mass and area ratio are disperse for aggregates of the same size (Fig. 5). The main differences between Figs. 10 and 11 occur with large values of Λ where the dispersion in area ratio in Fig. 10 acts to decrease self-aggregation rates compared to Fig. 11. This can be explained by the increased area term in Eq. (23) due to constraining the area distribution to be the same as spheres. The impact of mass dispersion therefore primarily affects self-aggregation rates for smaller values of Λ. Increasing $\alpha(\beta_m)$ mitigates this difference between ellipsoids and spheres. Overall, Fig. 11 shows very little if any difference in self-aggregation rates for both number and reflectivity except for very small values of Λ for the drag parameterization of Mitchell and Heymsfield (2005) and when $\alpha = -1$. Ellipsoids with the same mass distribution as spheres (Fig. 12) show similar differences for number as Fig. 10. The main difference between Figs. 10 and 12 is that Fig. 12 shows little variation of the difference in self-aggregation rates between ellipsoids and spheres whereas this difference monotonically increases in Fig. 10. Comparing all three figures suggests that the area term dominates at large values of Λ whereas the fall speed term dominates for small Λ values.

2) AGGREGATE ORIENTATION EFFECT

Figure 13 shows sensitivity tests for the self-aggregation rates when assuming horizontally oriented ellipsoids from Fig. 12 and randomly oriented ellipsoids when using the power-law parameterization from Fig. 2. The use of this parameterization for randomly oriented ellipsoids further decreases the projected area of ellipsoids by about 45% compared to horizontal orientations. The difference between these two tests can be explained by the projected area term in the collection kernel which is weighted by Ψ_{proj}. The fall speed term, as shown in Figs. 5–7, is primarily affected by particle mass which does not depend upon orientation. Therefore, the self-aggregation rates decrease based on factors that correspond to projected ellipse area: $\Psi_{\text{proj}} \approx 0.6$ for horizontally oriented aggregates and $\Psi_{\text{proj}} \approx 0.4$ for randomly oriented aggregates. The ability to expand the area term in the self-aggregation equations suggests that there are little to no nonlinear effects associated with orientation and self-aggregation rates.

4. An analytical correction parameterization for microphysics models

This section derives corrections to sedimentation and aggregation calculations that incorporate the effects of aggregate shapes while maintaining conventional power-law methodology. This allows for any microphysics model that prescribes assumed

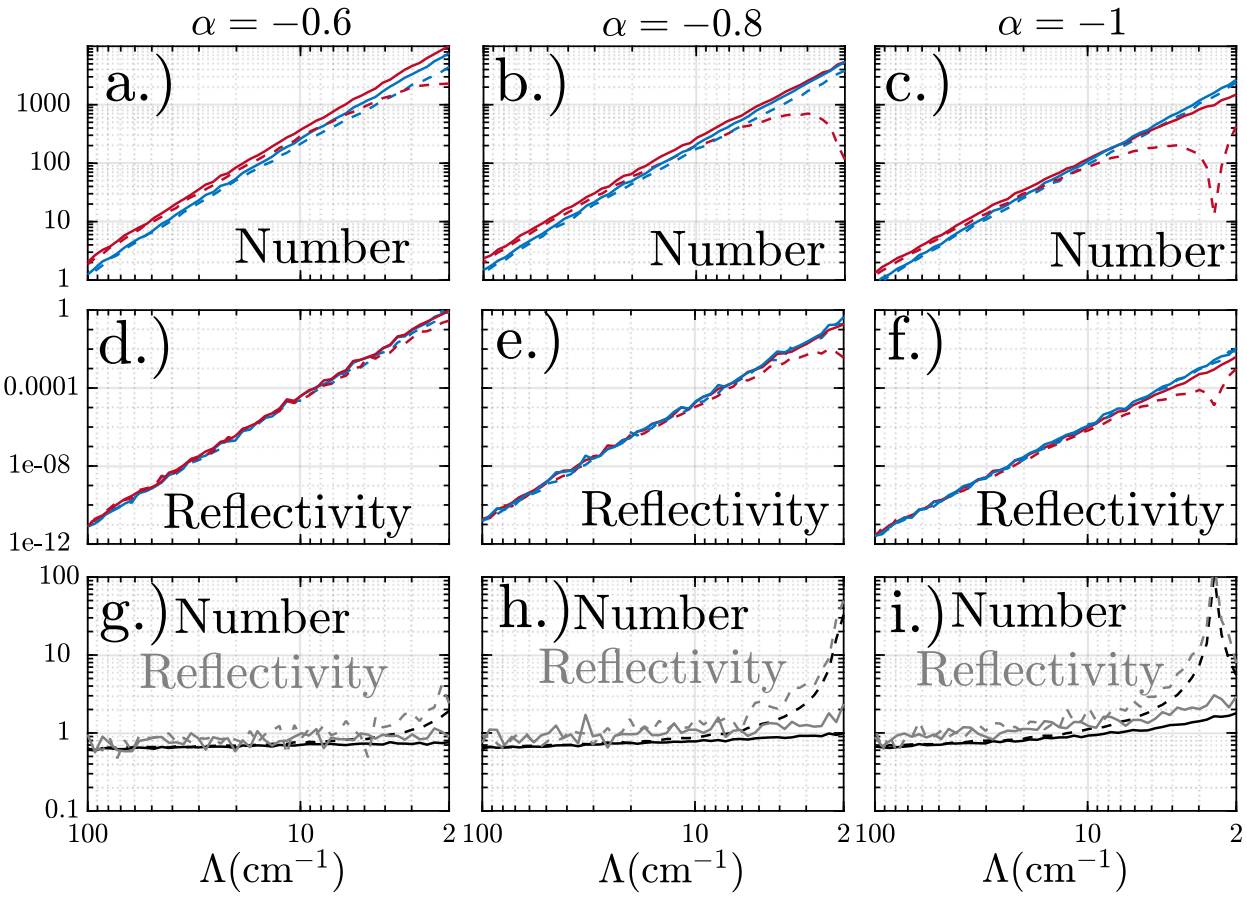

FIG. 10. Magnitude comparison of self-aggregation rates for (a)–(c) number and (d)–(f) reflectivity for spheres (red lines) and ellipsoids (blue lines) following Mitchell (1996) (solid) or Mitchell and Heymsfield (2005) (dashed) according to various Λ parameter values. Units are in cgs and ellipsoids are assumed to fall horizontally such that $\Psi_{ba} = 1.0$ and $\Psi_{ca} = 0$. (g)–(i) The ratio of self-aggregation rates (ellipsoids/spheres) for number (black) and reflectivity (gray). Calculations were performed by sampling each probability distribution 10 000 times. Ellipsoids of a particular size exhibit dispersion in both mass and projected area.

M–D and v_t–*D* relationships to exhibit a spread of masses and fall speeds while conserving mass. IWC consistency between the traditional (spherical/fractal) and the new (ellipsoidal) parameterizations is important because some in situ derived *M–D* relationships use IWC to constrain the parameterizations; using such relationships for a dispersion of aggregate shapes must necessarily yield the same IWC as that used for the relation. Here, the first two mass moments are constrained to be identical like in the previous sections. This allows for a single, nonlinear equation that relates the *M–D* sphere/fractal exponent β_{m_s} to the ellipsoidal *M–D* exponent β_m. This means that only β_{m_s} is necessary to find the corresponding β_m for an assumed bivariate ellipsoid distribution. For the ellipsoid distribution used in this paper and for horizontal orientations (i.e., $\Psi_{ba} = 1.0$ and $\Psi_{ca} = 0$), the resulting β_m is almost exactly linear from $1.4 \le \beta_{m_s} \le 2.6$ ($R^2 = 1$). This equation is given by

$$\beta_m = 1.016\beta_{m_s} - 0.1955. \tag{24}$$

A new prefactor can be derived by using Eq. (24) in the equation for mass mixing ratio q_i and a new characteristic semimajor dimension a_n can be derived by assuming a volume-weighted ellipsoidal density $\overline{\rho}_e$. The primary difference between Eq. (24) and that used in the results section is that the results section numerically solved for β_m whereas Eq. (24) provides an accurate and convenient linear fit.

Now, the new β_m can be used to find the corresponding power-law relationship for fall speed for an assumed β_{v_s}. As an example, the general assumption made by Mitchell (1996) and Mitchell and Heymsfield (2005) that $k_c = 1.0$ is assumed although $k_c = 0.5$ as used by Heymsfield and Westbrook (2010) could also be used. It is common for microphysics models to use *M–D* and v_t–*D* developed from different datasets. Therefore, to maintain generality, new fall speed relations are solved assuming that

$$v_{t_s} = \alpha_{v_s} a^{\beta_{v_s}} = \langle v_t \rangle_{\varphi_{ba},\varphi_{ca}} = \alpha_v a^{\beta_v} \left\langle \varphi_{ba}^{v_{ba}} \varphi_{ca}^{v_{ca}} \right\rangle = \alpha_v a^{\beta_v} \left\langle \varphi_{ba}^{2\overline{b}_m - 1/2} \varphi_{ca}^{\overline{b}_m} \right\rangle. \tag{25}$$

β_v can be solved by assuming $\overline{b}_m = \overline{b}_{m_s} \approx \overline{b}_{m_e}$ and $\beta_{\mathrm{AR}} = \beta_{\mathrm{AR}_s} \approx \beta_{\mathrm{AR}_e}$ so that

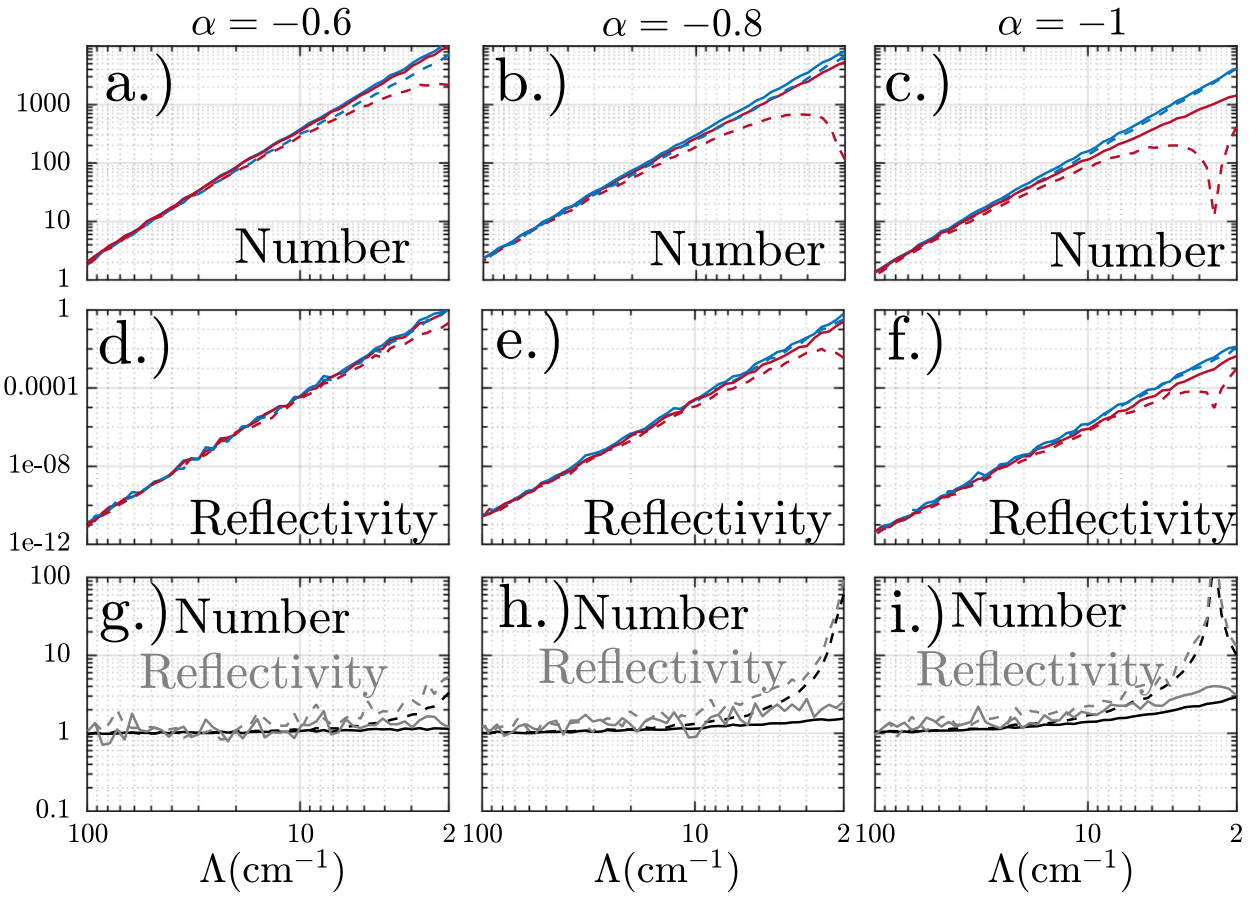

FIG. 11. As in Fig. 10, but with the same area ratio distribution between ellipsoids and spheres.

$$\overline{b}_m = \frac{\beta_{v_s} + 1}{\beta_{m_s} - \beta_{\mathrm{AR}}}, \tag{26a}$$

$$\beta_v = (\beta_m - \beta_{\mathrm{AR}})\overline{b}_m - 1. \tag{26b}$$

Finally, α_v can be solved by putting β_v in Eq. (25) and specifying a reference size, D_{ref}, based on the size interval used to derive the v_t–D relation. Equations (24)–(26) allow for the transformation of α_v and β_v without the need for any explicit drag parameterization scheme. A summary of all these conversions is given in Table 1 as well as relevant bulk quantities and closed-form expressions for aggregate self-aggregation rates using the variance fall speed approximation from Seifert et al. (2014). Notice that the extra gamma functions in Table 1 can generally be evaluated as time-independent constants for an assumed set of bivariate beta distribution parameters, α_{ba}, β_{ba}, and β_{cb}. Other bivariate distribution parameter sets would modify Eqs. (24)–(26).

An example of this procedure is shown in Fig. 14 where the fall speed relation from Fig. 1 in Zawadzki et al. (2010) is used to specify v_{t_s}. As shown in Fig. 1b from Zawadzki et al. (2010) and Fig. 3 from Brandes et al. (2008), the standard deviation of fall speeds for all sizes is approximately $\sigma = 0.2\,\mathrm{m\,s^{-1}}$. The new rescaled relation introduces approximately $\sigma = \pm 0.13\,\mathrm{m\,s^{-1}}$ about the mean based on the dispersion of aggregate shapes alone. This suggests that a dispersion of aggregate densities is necessary to capture the full range of fall speed variation. Interestingly enough, this estimate of σ happens to be quite close to older estimates provided by Sasyo and Matsuo (1980), who found that $\sigma \approx 0.12\,\mathrm{m\,s^{-1}}$ regardless of mass.

Normally, the shape-induced spread of fall speed has been ignored in the calculations for in situ observations. This has led to claims about a supposed lack of significant mass flux fall speed dispersion which, in turn, has historically served as the justification for Lagrangian spiral in situ cloud probe sampling of snow. This sampling technique assumes that the snow mass flux is contained within a narrow range of fall speeds, thus permitting a direct comparison of observed measurements from a slowly descending aircraft to a presumed population of steadily falling snowflakes. The justification for this approach appears to have stemmed from the theoretical analysis of Lo and Passarelli (1982), who provided an equation [their Eq. (4)] that describes the relative mass flux fall speed standard deviation (σ_m) for various values of β_{v_s}. For $\beta_{v_s} = 0.3$ [an assumption Lo and Passarelli (1982) use based on observational estimates at that time], their equation yields approximately $\sigma_m = 0.15\,\mathrm{m\,s^{-1}}$. However, there are at least three major

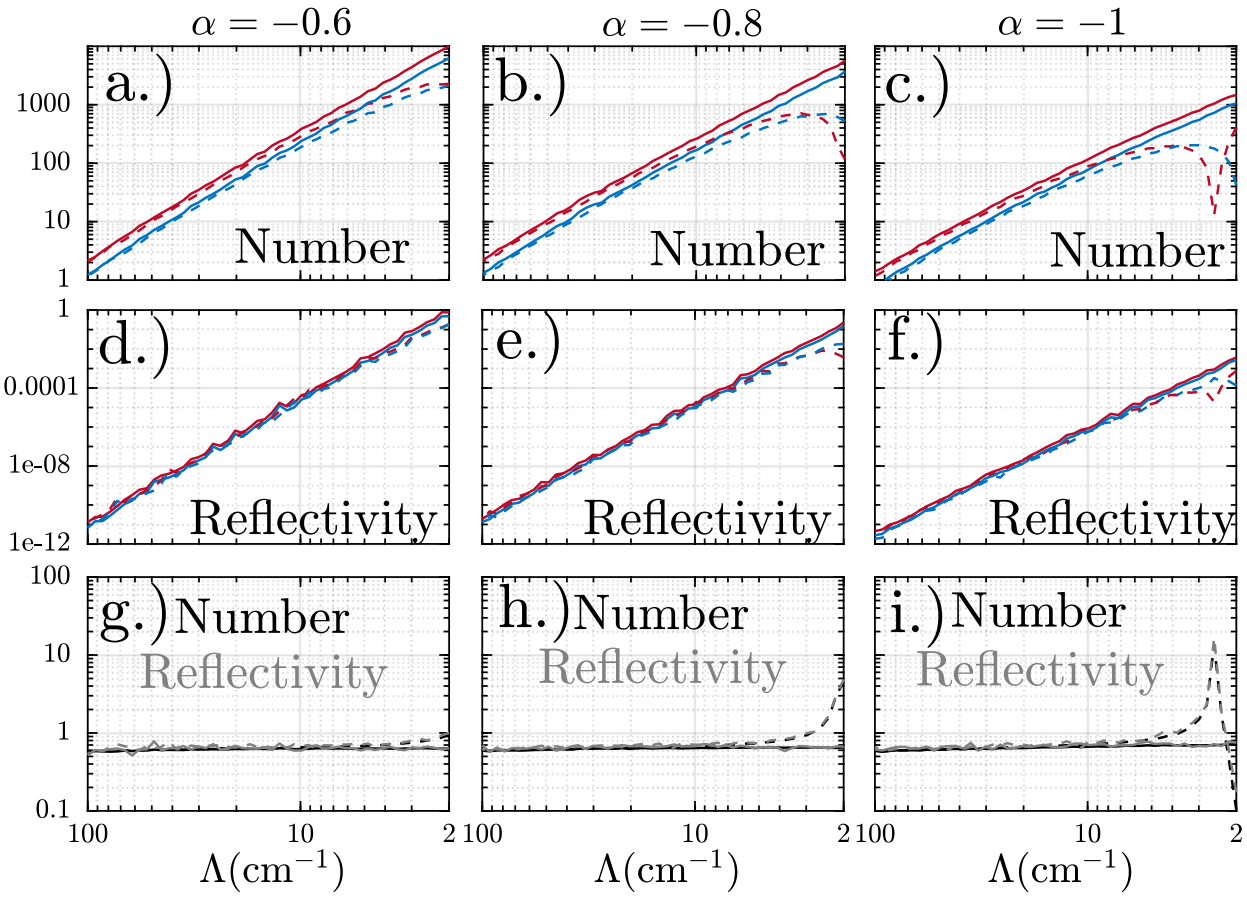

FIG. 12. As in Fig. 10, but with the same mass distribution between ellipsoids and spheres.

limitations of this equation. First, Lo and Passarelli (1982) assumes aggregates are homogeneous spheres with masses and fall speeds that are given in terms of melted diameters. Having such a large β_{m_s} skews their calculation of mass flux dispersion because higher values of β_{m_s} artificially weights mass flux to larger sizes. This is consistent with the results from Fig. 8 which shows that bulk fall speed quantities are significantly affected by β_m for both spheres and ellipsoids. More accurate estimates of $\beta_{m_s} \approx 2.0$ will therefore allow for the fall speed dispersion to produce a more profound effect on the mass flux dispersion. Second, their equation necessarily ignores the fall speed and mass dispersion for particles of the same size. In contrast, the equations provided in this work introduce an additional set of gamma functions in Eq. (4) from Lo and Passarelli (1982) that they do not include. Without these additional factors, Eq. (4) in Lo and Passarelli (1982) represents an underestimate of the true mass flux dispersion even if the M–D and v_t–D relationships are accurate. Finally, more recent estimates of β_{v_s} (e.g., Zawadzki et al. 2010) seem to suggest that β_{v_s} is lower in value than what Lo and Passarelli (1982) had originally assumed. The traditional power-law framework suggests that the fall speed distribution should narrow for smaller values of β_{v_s} even though the variation of aggregate shapes negates this narrowing as demonstrated in Figs. 5 and 6. The question then becomes, How much does the mass flux fall speed dispersion change when using the above shape parameterization correction?

Figure 15 shows a comparison of σ_m using Eq. (4) from Lo and Passarelli (1982) and using the analytical correction parameterization from Eqs. (24)–(26). β_{m_s} is varied for reasonable values of β_{m_s} as well as for $\beta_{m_s} = 3.0$ as assumed by Lo and Passarelli (1982). Ellipsoidal aggregates universally produce larger mass flux fall speed dispersion for the same β_{m_s} and β_{v_s} values. The difference between the ellipsoid and sphere mass flux dispersion increases dramatically as β_{v_s} decreases. For the assumed value of $\beta_{v_s} = 0.3$ used by Lo and Passarelli (1982), the introduction of ellipsoidal shapes increases the mass flux fall speed dispersion by approximately 25% from $\sigma_m \approx 0.15\ \mathrm{m\,s^{-1}}$ to $\sigma_m \approx 0.19\ \mathrm{m\,s^{-1}}$. Decreasing β_{m_s} further exacerbates this discrepancy to more than 50% of that estimated by Lo and Passarelli (1982) where σ_m is between approximately 0.25 and $0.28\ \mathrm{m\,s^{-1}}$. Lo and Passarelli (1982) provided an example calculation where the mean mass flux fall speed equals $1.05\ \mathrm{m\,s^{-1}}$. In this case, their estimate of $\sigma_m \approx 0.15\ \mathrm{m\,s^{-1}}$ would yield a range of mass flux fall speeds between 0.74 and $1.37\ \mathrm{m\,s^{-1}}$ ($\pm 2\sigma_m$) which they claimed contained the vast majority of mass flux.

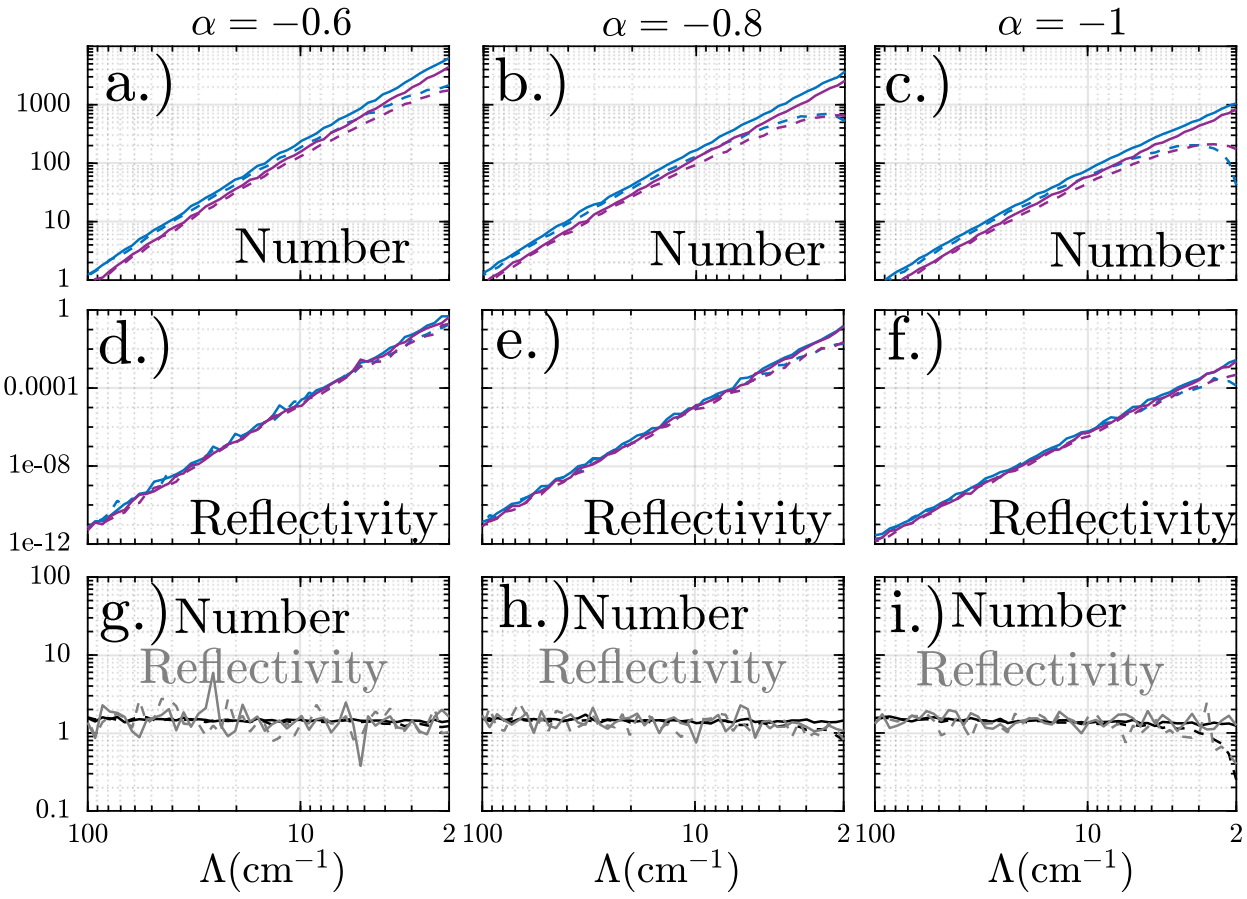

FIG. 13. As in Fig. 12, but with horizontally oriented ellipsoidal aggregates (blue) and randomly oriented ellipsoidal aggregates (purple). (g)–(i) Horizontally oriented ellipsoids over randomly oriented ellipsoids. Only Mitchell (1996) (solid) and Mitchell and Heymsfield (2005) (dashed) drag parameters are shown.

However, the estimate of the present work suggests that σ_m would be at least 0.25 m s^{-1} for $\beta_{v_s} = 0.3$. Therefore, the full range of mass flux fall speeds (as estimated by $\pm 2\sigma_m$) would span approximately 1.0 m s^{-1}. As a result, the variation of fall speeds responsible for the mass flux would approximately equal the mean mass flux fall speed itself. Moreover, the mass flux dispersion difference between ellipsoids and spheres increases dramatically as β_{v_s} decreases. For $\beta_{v_s} \approx 0.15$, as observe by Zawadzki et al. (2010), ellipsoids yield σ_m that is more than 100% larger than that predicted by Lo and Passarelli (1982).

5. Conclusions

Some authors (e.g., Zawadzki et al. 2010; Szyrmer and Zawadzki 2010) have emphasized that fall speed should be parameterized according to a measure of size that decreases the observed spread. However, this study suggests that future efforts should embrace rather than skirt the inherent fall speed variability. Ignoring this variability leads to incorrect estimates of sedimentation and aggregation where the fall speed distribution unphysically narrows for larger sizes (smaller slope parameters) which would further influence the subsequent growth of the aggregates themselves. As a result, the conventional power-law framework has obfuscated the physical understanding of fall speed dispersion. For instance, much of what is known about aggregates and their evolution has resulted from studies that attempt to observe a population of these particles as they fall. However, incorporation of shape dispersion increases the mean relative mass flux fall speed dispersion by more than 100%. The result of this increase in fall speed dispersion suggests that the mass flux contribution from each particle is not restricted to a narrow range of fall speeds as stated by Lo and Passarelli (1982). The increase in relative fall speed distribution dispersion from ellipsoids also negates the hypothesized distribution narrowing proposed by Mitchell and Heymsfield (2005). This suggests that self-aggregation rates remain large and even increase with decreasing values of Λ. As a result, other ice mechanisms such as collisional breakup or rime splintering must take place in order to prevent Λ from continuously decreasing.

Nonlinearities among microphysical parameters complicate the use of static M–D and v_t–D relationships because these relationships are derived without consideration of shape and

TABLE 1. Relations between original (spherical/fractal aggregate) parameters and moments and new (bivariate ellipsoidal) parameters and moments for static M–D and v_t–D relationships where $k_c = 1.0$, $\Psi_{ba} = 1.0$, and $\Psi_{ca} = 0$ (horizontal orientations).

Parameter	Original (spheres/fractals)	New (Ellipsoids)
α_{ba}	—	6.9793
β_{ba}	—	4.3502
β_{cb}	—	5.3437
β_{AR}	-0.12	-0.12
β_m	β_{m_s}	$1.016\beta_{m_s} - 0.1955$
α_m	α_{m_s}	$\frac{q_i}{N_i} a_n^{-\beta_m} \frac{\Gamma(\nu)}{\Gamma(\nu+\beta_m)} \frac{(\alpha_{ba}+\beta_{ba}+1)(\alpha_{ba}+\beta_{ba}+\beta_{cb})}{\alpha_{ba}(\alpha_{ba}+1)}$
a_n	$\left[\frac{q_i}{\alpha_{m_s} N_i} \frac{\Gamma(\nu)}{\Gamma(\nu+\beta_{m_s})}\right]^{1/\beta_{m_s}}$	$\left[\frac{q_i}{\frac{4}{3} N_i \pi \overline{\rho}_e} \frac{\Gamma(\nu)}{\Gamma(\nu+\beta_m)} \frac{(\alpha_{ba}+\beta_{ba}+1)(\alpha_{ba}+\beta_{ba}+\beta_{cb})}{\alpha_{ba}(\alpha_{ba}+1)}\right]^{1/\beta_m}$
$\overline{b}_m$	$\frac{\beta_{v_s}+1}{\beta_{m_s}-\beta_{\mathrm{AR}}}$	$\frac{\beta_{v_s}+1}{\beta_{m_s}-\beta_{\mathrm{AR}}}$
β_v	β_{v_s}	$(\beta_m - \beta_{\mathrm{AR}})\overline{b}_m - 1$
α_v	α_{v_s}	$\alpha_{v_s} a_{\mathrm{ref}}^{\beta_{v_s}-\beta_v} \frac{\Gamma(\alpha_{ba})\Gamma(\alpha_{ba}+\beta_{ba}+\beta_{cb}+\upsilon_{ca})\Gamma(\alpha_{ba}+\beta_{ba}+\upsilon_{ba}+\upsilon_{ca})}{\Gamma(\alpha_{ba}+\beta_{ba}+\beta_{cb})\Gamma(\alpha_{ba}+\beta_{ba}+\upsilon_{ca})\Gamma(\alpha_{ba}+\upsilon_{ba}+\upsilon_{ca})}$
υ_{ba}	—	$2\overline{b}_m - \frac{1}{2}$
υ_{ca}	—	$\overline{b}_m$
$A(a_n)$	πa_n^2	πa_n^2
$m(a_n)$	$\alpha_{m_s} a_n^{\beta_{m_s}}$	$\alpha_m a_n^{\beta_m}$
$v_t(a_n)$	$\alpha_{v_s} a_n^{\beta_{v_s}}$	$\alpha_v a_n^{\beta_v}$
$\overline{\Delta v_t}_{xy}$	$\frac{v_t(a_n)}{\Gamma(\nu+2)} \sqrt{\sum_{k=0}^{2} \binom{2}{k} (-1)^k \Gamma[\nu+2+(2-k)\beta_{v_s}]\Gamma(\nu+2+k\beta_{v_s})}$	$\frac{v_t(a_n)}{\Gamma(\nu+2)} \frac{\alpha_{ba}}{\alpha_{ba}+\beta_{ba}} \sqrt{\sum_{k=0}^{2} \binom{2}{k} (-1)^k \Gamma[\nu+2+(2-k)\beta_v]\Gamma(\nu+2+k\beta_v)\langle \varphi_{ba}^{(2-k)\upsilon_{ba}} \varphi_{ca}^{(2-k)\upsilon_{ca}} \rangle \langle \varphi_{ba}^{k\upsilon_{ba}} \varphi_{ca}^{k\upsilon_{ca}} \rangle}$
$\overline{\Delta v_t}_{tz\,xy}$	$\frac{v_t(a_n)}{\Gamma(\nu+2+\beta_{m_s})} \sqrt{\sum_{k=0}^{2} \binom{2}{k} (-1)^k \Gamma[\nu+2+\beta_{m_s}+(2-k)\beta_{v_s}]\Gamma(\nu+2+\beta_{m_s}+k\beta_{v_s})}$	$\frac{v_t(a_n)}{\Gamma(\nu+\beta_m+2)} \frac{\alpha_{ba}(\alpha_{ba}+1)(\alpha_{ba}+2)}{(\alpha_{ba}+\beta_{ba}+1)(\alpha_{ba}+\beta_{ba}+2)(\alpha_{ba}+\beta_{ba}+\beta_{cb})}$ $\times \sqrt{\sum_{k=0}^{2} \binom{2}{k} (-1)^k \Gamma[\nu+2+\beta_m+(2-k)\beta_v]\Gamma(\nu+2+\beta_m+k\beta_v)\langle \varphi_{ba}^{1+(2-k)\upsilon_{ba}} \varphi_{ca}^{1+(2-k)\upsilon_{ca}} \rangle \langle \varphi_{ba}^{1+k\upsilon_{ba}} \varphi_{ca}^{1+k\upsilon_{ca}} \rangle}$

Moments/bulk quantities	Original (spheres/fractals)	New (ellipsoids)
Number mixing ratio	N_i	N_i
IWC	$\frac{N_i}{\rho_a} m(a_n) \frac{\Gamma(\nu+\beta_{m_s})}{\Gamma(\nu)}$	$\frac{N_i}{\rho_a} m(a_n) \frac{\Gamma(\nu+\beta_m)}{\Gamma(\nu)} \frac{\alpha_{ba}(\alpha_{ba}+1)}{(\alpha_{ba}+\beta_{ba}+1)(\alpha_{ba}+\beta_{ba}+\beta_{cb})}$
Number-weighted fall speed	$v_t(a_n) \frac{\Gamma(\nu+\beta_{v_s})}{\Gamma(\nu)}$	$v_t(a_n) \frac{\Gamma(\nu+\beta_v)}{\Gamma(\nu)} \frac{\Gamma(\alpha_{ba}+\beta_{ba}+\beta_{cb})\Gamma(\alpha_{ba}+\beta_{ba}+\upsilon_{ca})\Gamma(\alpha_{ba}+\upsilon_{ba}+\upsilon_{ca})}{\Gamma(\alpha_{ba})\Gamma(\alpha_{ba}+\beta_{ba}+\beta_{cb}+\upsilon_{ca})\Gamma(\alpha_{ba}+\beta_{ba}+\upsilon_{ba}+\upsilon_{ca})}$
Snow precipitation rate	$\frac{N_i}{\rho_a} m(a_n) v_t(a_n) \frac{\Gamma(\nu+\beta_{m_s}+\beta_{v_s})}{\Gamma(\nu)}$	$\frac{N_i}{\rho_a} m(a_n) v_t(a_n) \frac{\Gamma(\nu+\beta_m+\beta_v)}{\Gamma(\nu)} \frac{\Gamma(\alpha_{ba}+\beta_{ba}+\beta_{cb})\Gamma(\alpha_{ba}+\beta_{ba}+\upsilon_{ca}+1)\Gamma(\alpha_{ba}+\upsilon_{ba}+\upsilon_{ca}+2)}{\Gamma(\alpha_{ba})\Gamma(\alpha_{ba}+\beta_{ba}+\beta_{cb}+\upsilon_{ca}+1)\Gamma(\alpha_{ba}+\beta_{ba}+\upsilon_{ba}+\upsilon_{ca}+2)}$

TABLE 1. (*Continued*)

Moments/bulk quantities	Original (spheres/fractals)	New (ellipsoids)
Snow number self-aggregation rate	$-\frac{1}{2}E_{\text{agg}}\overline{\Delta v_{i,xy}}A(a_n)\frac{N_t^2}{\Gamma^2(\nu)}\sum_{k=0}^{2}\binom{2}{k}\Gamma\left(\nu+\frac{2-k}{2}\right)\Gamma\left(\nu+\frac{k}{2}\right)$	$-\frac{1}{2}\pi E_{\text{agg}}\overline{\Delta v_{i,xy}}A(a_n)\frac{N_t^2}{\Gamma^2(\nu)}\frac{\Gamma^2(\alpha_{ba}+\beta_{ba})}{\Gamma^2(\alpha_{ba})}\sum_{k=0}^{2}\binom{2}{k}\Gamma\left(\nu+\frac{2-k}{2}\right)\Gamma\left(\nu+\frac{k}{2}\right)$ $\times\frac{\Gamma\left(\alpha_{ba}+\frac{2-k}{2}\right)\Gamma\left(\alpha_{ba}+\frac{k}{2}\right)}{\Gamma\left(\alpha_{ba}+\beta_{ba}+\frac{2-k}{2}\right)\Gamma\left(\alpha_{ba}+\beta_{ba}+\frac{k}{2}\right)}$
Snow reflectivity self-aggregation rate	$E_{\text{agg}}\overline{\Delta v_{iz,xy}}m^2(a_n)A(a_n)\frac{N_t^2}{\Gamma^2(\nu)}\sum_{k=0}^{2}\binom{2}{k}\Gamma\left(\nu+\beta_{m_s}+\frac{2-k}{2}\right)\Gamma\left(\nu+\beta_{m_s}+\frac{k}{2}\right)$	$E_{\text{agg}}\overline{\Delta v_{iz,xy}}m^2(a_n)A(a_n)\frac{N_t^2}{\Gamma^2(\nu)}\frac{\Gamma^2(\alpha_{ba}+\beta_{ba}+1)}{(\alpha_{ba}+\beta_{ba}+\beta_{cb})^2\Gamma^2(\alpha_{ba})}$ $\times\sum_{k=0}^{2}\binom{2}{k}\Gamma\left(\nu+\beta_m+\frac{2-k}{2}\right)\frac{\Gamma\left(\alpha_{ba}+3-\frac{k}{2}\right)\Gamma\left(\alpha_{ba}+2+\frac{k}{2}\right)}{\Gamma\left(\alpha_{ba}+\beta_{ba}+3-\frac{k}{2}\right)\Gamma\left(\alpha_{ba}+\beta_{ba}+2+\frac{k}{2}\right)}$

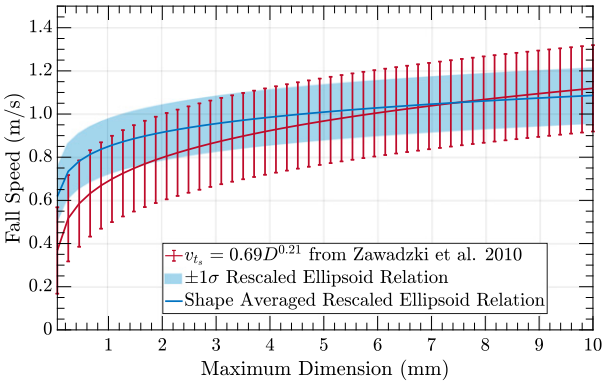

FIG. 14. Comparison of a typical v_t–D relationship from Zawadzki et al. (2010) and an ellipsoid shape rescaled version using the methodology from section 4. Error bars (illustrating $\sigma = 0.2\,\text{m s}^{-1}$) represent the approximate observed spread shown in Fig. 1 from Zawadzki et al. (2010). Shaded region represents $\pm 1\sigma$ produced from the influence of using a distribution of ellipsoids rather than spheres. A reference size of $D = 7.5$ mm was used to scale the new relation and $\beta_{m_s} \approx 1.80$ [$\alpha = -1$ using the hybrid area-ratio parameterization of Heymsfield et al. (2002a)].

density variation for a particular size. The bivariate beta parameters observed by Dunnavan et al. (2019) and used in this study suggest that $\langle \varphi_{ba}\varphi_{ca} \rangle \approx 0.27$ and $\langle \varphi_{ba}^2\varphi_{ca}^2 \rangle \approx 0.08$. These additional factors impact IWC and reflectivity, respectively. Often M–D relationships can implicitly include this factor when using observations to estimate the prefactor, α_m. However, ignoring this factor could therefore alter calculations of the second mass moment (reflectivity) when analytically integrating PSDs. Many microphysics models predict the second mass moment when comparing NWP models with radar observations or will use this moment to analytically estimate Λ (e.g., Passarelli 1978; Mitchell 1988; Mitchell et al. 2006). Traditional M–D relations do not explicitly constrain the second mass moment. Therefore, it is not clear what would happen to self-aggregation rates for a known appropriate second mass moment. Constraining the first two mass moments between ellipsoids and spheres clearly leads to a cancellation of effects between fall speed and projected area such that the self-aggregation rates are lower than that of spheres for large Λ (where ellipsoidal projected area is smaller than spheres) but increases to become larger than spheres for small Λ (where fall speed dispersion becomes much larger than spheres). Other ρ_e parameterizations could in theory yield more significant differences in fall speed quantities and self-aggregation rates.

The current study illustrates that the power-law framework can be expanded to include convolutions of various distributions. Distribution moments for any power-law combination of other random variables [Eq. (4)] yield gamma functions as in traditional bulk microphysics models. While the functional form of the underlying distributions remains quite complicated (see Table 1 in supplementary materials), distribution moments themselves are comparatively simple and easy to implement in both bulk and bin microphysics models. Incorporating additional probability distributions in microphysical model calculations therefore allows NWP and

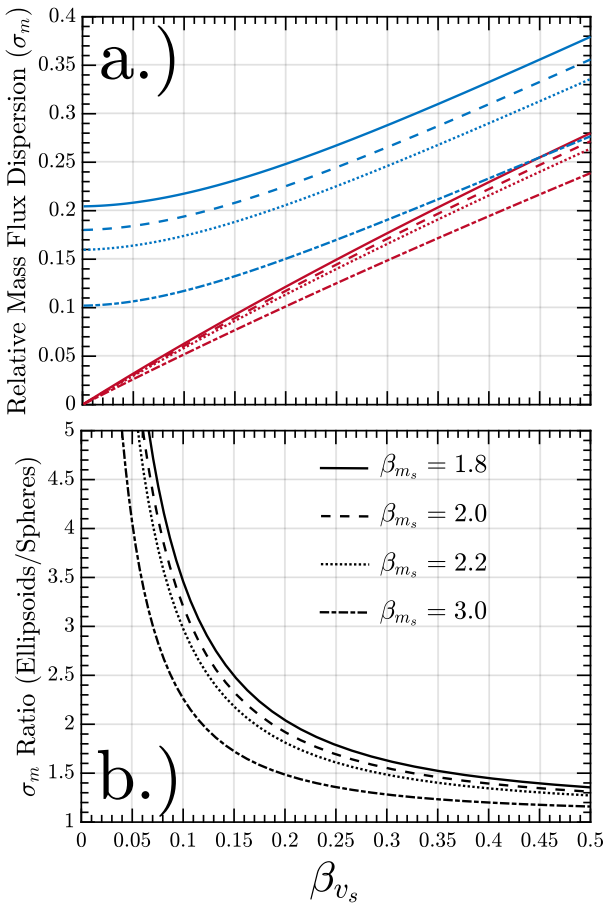

FIG. 15. (a) Comparison of relative mass flux fall speed dispersion [based on Eq. (4) from Lo and Passarelli (1982)] for spheres (red) and for distribution equivalent ellipsoids (blue) based on an assumed fall speed power-law exponent for spheres (β_{v_s}). (b) Ratio of relative dispersions (ellipsoids/spheres) from (a). Line styles represent different values of β_{m_s}.

climate models to overcome mathematical limitations imposed by singular power laws.

Acknowledgments. The author thanks Jerry Harrington, Hans Verlinde, and Jacob Carlin for their important advice and suggestions as well as Matthew Kumjian and Alexander Ryzhkov for their willingness to use their project funding resources for this independent work. This research was supported by the U.S. Department of Energy's Atmospheric Science Program Atmospheric System Research, an Office of Science, Office of Biological and Environmental Research program, under Grant DE-SC0018933. Additional funding was provided by NOAA/Office of Oceanic and Atmospheric Research under NOAA–University of Oklahoma Cooperative Agreement NA16OAR4320115, U.S. Department of Commerce and through the NSF Grant 1841246.

Data availability statement. All of the data used in this paper can be reproduced using MATLAB codes available from the author upon request.

APPENDIX

List of Symbols

a	a-axis semilength of ellipsoidal ice particle
$\overline{a}_m$	Best number–weighted Reynolds number power-law coefficient [Eq. (9b)]
a_n	Characteristic a-axis length for size spectrum
a_o	Drag parameter in Eqs. (9a) and (9b)
A_{circ}	Sphere/fractal projected circle area (see Fig. 1)
A_{part}	Projected particle area (see Fig. 1)
A_{proj}	Projected ellipse area (see Fig. 1)
$A_r\|_{\text{ellip}}$	Ellipsoid projected ellipse area ratio, $A_r\|_{\text{ellip}} = A_{\text{part}}/A_{\text{ellip}} = A_r\|_{\text{sph}}\varphi_{ba}^{-\Psi_{ba}}\varphi_{ca}^{-\Psi_{ca}}$ (see Fig. 1)
$A_r\|_{\text{sph}}$	Sphere/fractal projected area ratio, $A_r\|_{\text{sph}} = A_{\text{part}}/A_{\text{circ}}$ (see Fig. 1)
α	Sphere/fractal effective density exponent parameter from Heymsfield et al. (2002b) [Eq. (13)]
α_{AR}	Area ratio power-law coefficient, $\alpha_{\text{AR}} = 2^{\varsigma}/\pi$
α_{ba}	Bivariate beta distribution parameter
α_m	Mass–dimensional power-law prefactor coefficient for ellipsoid aggregates
α_{m_s}	Mass–dimensional power-law prefactor coefficient for sphere/fractal aggregates where $\alpha_{m_s} = (4/3)\pi\alpha_{\rho_s}$
α_{ρ_s}	Mass–dimensional power-law prefactor coefficient for sphere/fractal aggregates where $\alpha_{\rho_s} = 2^{\beta_{\rho_s}}\pi k\sigma^n$
α_v	Ellipsoid fall speed–dimensional power-law coefficient where $\alpha_v = (1/2)(\eta_a/\rho_a)\overline{a}_m\alpha_X^{\overline{b}_m}$
α_{v_s}	Sphere fall speed–dimensional power-law coefficient
α_X	Ellipsoid Best number power-law coefficient where $\alpha_X = [8g\rho_a/(\pi\eta_a^2)]\alpha_m\alpha_{\text{AR}}^{-k_c}$
b	b-axis semilength of ellipsoidal ice particle
$\overline{b}_m$	Number-weighted Best number Reynolds number power-law exponent [Eq. (9a)]
b_o	Drag parameter in Eqs. (9a) and (9b)
$B(a, b)$	Beta function, $B(a, b) = [\Gamma(a)\Gamma(b)]/[\Gamma(a + b)]$
β_{AR}	Area ratio power-law exponent, $\beta_{\text{AR}} = \varsigma - 2$
β_{ba}	Bivariate beta distribution parameter
β_{cb}	Bivariate beta distribution parameter
β_m	Ellipsoid mass–dimensional power-law exponent where $\beta_m = 3 + \beta_{\rho_e}$
β_{m_s}	Mass–dimensional power-law exponent for spheres or equivalently described as a "fractal dimension" where $\beta_{m_s} = \beta_{\rho_s} + 3$
β_{ρ_e}	Ellipsoid effective-density power-law exponent
β_{ρ_s}	Sphere effective-density power-law exponent where $\beta_{\rho_s} = n(\varsigma - 2) + \alpha$
β_v	Ellipsoid fall speed–dimensional power-law exponent where $\beta_v = \beta_X\overline{b}_m - 1$
β_{v_s}	Sphere fall speed–dimensional power-law exponent
β_X	Ellipsoid Best number power-law exponent [Eq. (18)] where $\beta_X = \beta_m - k_c\beta_{\text{AR}}$
$\binom{n}{k}$	Binomial coefficients
c	c-axis semilength of ellipsoidal ice particle
C_o	Drag parameterization constant [Eqs. (9a) and (9b)]
C_1	Drag parameterization constant [Eqs. (9a) and (9b)]

C_2	Drag parameterization constant [Eqs. (9a) and (9b)]
D	Particle maximum dimension, $D = 2a$
D_n	Characteristic maximum dimension
δ_0	Drag parameterization constant [Eqs. (9a) and (9b)]
Δ_t	Khvorostyanov and Curry (2005) turbulence correction term [Eqs. (9a) and (9b)]
$\overline{\Delta v_{txy}}$	Number-weighted fall speed difference approximation for $\lvert v_{t_x} - v_{t_y}\rvert$ following Seifert et al. (2014) (see Table 1)
$\overline{\Delta v_{tzxy}}$	Reflectivity-weighted fall speed difference approximation for $\lvert v_{t_x} - v_{t_y}\rvert$ following Seifert et al. (2014) (see Table 1)
E_{agg}	Aggregation efficiency
η_a	Dynamic viscosity for air
$\Gamma(x)$	The gamma function
k	Area ratio coefficient in Eq. (13)
k_c	Area ratio correction exponent Eq. (10)
$K(x, y)$	Aggregation collection kernel
L	Maximum span of aggregate projection
Λ	PSD slope parameter
m	Ice particle mass
μ	PSD shape parameter, $\mu = \nu - 1$
M_r	rth moment of the particle mass distribution $n(x, t)$
n	Area ratio exponent parameter in Eq. (13) where $n = 1.5$
N_0	Size distribution intercept parameter
N_i	Ice particle number mixing ratio
N_{Re}	Reynolds number
$n(D)$ or $n(x, t)$	Particle size distribution or particle mass distribution
$\tilde{n}(\varphi_{ba}, \varphi_{ca})$	Bivariate beta ellipsoid aspect ratio probability distribution
φ	First Euler angle rotation
φ_{bc}	Ellipsoid aspect ratio b/c
φ_{ba}	Ellipsoid aspect ratio b/a
ψ	Third Euler angle rotation
$\overline{\psi}_t$	Khvorostyanov and Curry (2005) turbulence correction term [Eqs. (9a) and (9b)]
Ψ_{proj}	Projected ellipse area geometric factor
Ψ_{ba}	Projected ellipse area geometric factor power-law exponent
Ψ_{ca}	Projected ellipse area geometric factor power-law exponent
ν	PSD shape parameter, $\nu = \mu + 1$
q_i	Ice particle mass mixing ratio
R	Particle sphere radius, $R = a$
ρ_a	Air density
ρ_e	Effective ellipsoid aggregate density
ρ_s	Effective sphere aggregate density
σ	A_{part} power-law coefficient from Mitchell (1996) [Eq. (11)]
σ_m	Aggregate relative mass flux fall speed dispersion
$\mathfrak{s}$	A_{part} power-law exponent from Mitchell (1996) [Eq. (11)]
θ	Second Euler angle rotation
v_{ba}	Ellipsoid fall speed φ_{ba} exponent: $v_{ba} = \chi_{ba}\overline{b}_m - \psi_{ba}/2$
v_{ca}	Ellipsoid fall speed φ_{ca} exponent: $v_{ca} = \chi_{ca}\overline{b}_m - \psi_{ca}/2$
V_e	Ice ellipsoid volume
v_t	Terminal particle fall speed
X	Best or Davies number
$\overline{X}$	Number-weighted Best number
χ_{ba}	Best number φ_{ba} exponent: $\chi_{ba} = k_c\Psi_{ba}$ if using Eq. (14) and $\chi_{ba} = k_c\Psi_{ba} + 1$ if using Eq. (15)
χ_{ca}	Best number φ_{ca} exponent: $\chi_{ca} = k_c\Psi_{ca}$ if using Eq. (14) and $\chi_{ca} = k_c\Psi_{ca} + 1$ if using Eq. (15)
ξ	A general microphysical quantity, e.g., mass (m)
ζ	A general power-law exponent

REFERENCES

Abraham, F. F., 1970: Functional dependence of the drag coefficient of a sphere on Reynolds number. *Phys. Fluids*, **13**, 2194, https://doi.org/10.1063/1.1693218.

Bleck, R., 1970: A fast, approximative method for integrating the stochastic coalescence equation. *J. Geophys. Res.*, **75**, 5165–5171, https://doi.org/10.1029/JC075i027p05165.

Blumenfeld, R., and B. B. Mandelbrot, 1997: Lévy dusts, Mittag-Leffler statistics, mass fractal lacunarity, and perceived dimension. *Phys. Rev.*, **56E**, 112–118, https://doi.org/10.1103/PhysRevE.56.112.

Böhm, J., 1989: A general equation for the terminal fall speed of solid hydrometeors. *J. Atmos. Sci.*, **46**, 2419–2427, https://doi.org/10.1175/1520-0469(1989)046<2419:AGEFTT>2.0.CO;2.

——, 1992: A general hydrodynamic theory for mixed-phase microphysics. Part III: Riming and aggregation. *Atmos. Res.*, **28**, 103–123, https://doi.org/10.1016/0169-8095(92)90023-4.

Brandes, E. A., K. Ikeda, G. Zhang, M. Schönhuber, and R. M. Rasmussen, 2007: A statistical and physical description of hydrometeor distributions in Colorado snowstorms using a video disdrometer. *J. Appl. Meteor. Climatol.*, **46**, 634–650, https://doi.org/10.1175/JAM2489.1.

——, ——, G. Thompson, and M. Schönhuber, 2008: Aggregate terminal velocity/temperature relations. *J. Appl. Meteor. Climatol.*, **47**, 2729–2736, https://doi.org/10.1175/2008JAMC1869.1.

Connolly, P. J., C. Emersic, and P. R. Field, 2012: A laboratory investigation into the aggregation efficiency of small ice crystals. *Atmos. Chem. Phys.*, **12**, 2055–2076, https://doi.org/10.5194/acp-12-2055-2012.

Drake, R. L., 1972: The scalar transport equation of coalescence theory: Moments and kernels. *J. Atmos. Sci.*, **29**, 537–547, https://doi.org/10.1175/1520-0469(1972)029<0537:TSTEOC>2.0.CO;2.

Dunnavan, E. L., Z. Jiang, J. Y. Harrington, J. Verlinde, K. Fitch, and T. J. Garrett, 2019: The shape and density evolution of snow aggregates. *J. Atmos. Sci.*, **76**, 3919–3940, https://doi.org/10.1175/JAS-D-19-0066.1.

Field, P. R., and A. J. Heymsfield, 2003: Aggregation and scaling of ice crystal size distributions. *J. Atmos. Sci.*, **60**, 544–560, https://doi.org/10.1175/1520-0469(2003)060<0544:AASOIC>2.0.CO;2.

Fox, C., 1961: The G and H functions as symmetrical Fourier kernels. *Trans. Amer. Math. Soc.*, **98**, 395–429, https://doi.org/10.2307/1993339.

Garrett, T. J., S. E. Yuter, C. Fallgatter, K. Shukurko, S. R. Rhodes, and J. L. Endries, 2015: Orientations and aspect ratios of falling snow. *Geophys. Res. Lett.*, **42**, 4617–4622, https://doi.org/10.1002/2015GL064040.

Harrington, J. Y., K. Sulia, and H. Morrison, 2013: A method for adaptive habit prediction in bulk microphysical models.

Part I: Theoretical development. *J. Atmos. Sci.*, **70**, 349–364, https://doi.org/10.1175/JAS-D-12-040.1.

Heymsfield, A. J., and L. M. Miloshevich, 2003: Parameterizations for the cross-sectional area and extinction of cirrus and stratiform ice cloud particles. *J. Atmos. Sci.*, **60**, 936–956, https://doi.org/10.1175/1520-0469(2003)060<0936:PFTCSA>2.0.CO;2.

——, and C. D. Westbrook, 2010: Advances in the estimation of ice particle fall speeds using laboratory and field measurements. *J. Atmos. Sci.*, **67**, 2469–2482, https://doi.org/10.1175/2010JAS3379.1.

——, A. Bansemer, P. R. Field, S. L. Durden, J. L. Stith, J. E. Dye, W. Hall, and C. A. Grainger, 2002a: Observations and parameterizations of particle size distributions in deep tropical cirrus and stratiform precipitation clouds: Results from in situ observations in TRMM field campaigns. *J. Atmos. Sci.*, **59**, 3457–3491, https://doi.org/10.1175/1520-0469(2002)059<3457:OAPOPS>2.0.CO;2.

——, S. Lewis, A. Bansemer, J. Iaquinta, L. M. Miloshevich, M. Kajikawa, C. Twohy, and M. R. Poellot, 2002b: A general approach for deriving the properties of cirrus and stratiform ice cloud particles. *J. Atmos. Sci.*, **59**, 3–29, https://doi.org/10.1175/1520-0469(2002)059<0003:AGAFDT>2.0.CO;2.

Hogan, R. J., L. Tian, P. R. A. Brown, C. D. Westbrook, A. J. Heymsfield, and J. D. Eastment, 2012: Radar scattering from ice aggregates using the horizontally aligned oblate spheroid approximation. *J. Appl. Meteor. Climatol.*, **51**, 655–671, https://doi.org/10.1175/JAMC-D-11-074.1.

Jensen, A. A., J. Y. Harrington, H. Morrison, and J. A. Milbrandt, 2017: Predicting ice shape evolution in a bulk microphysics model. *J. Atmos. Sci.*, **74**, 2081–2104, https://doi.org/10.1175/JAS-D-16-0350.1.

Jiang, Z., J. Verlinde, E. E. Clothiaux, K. Aydin, and C. Schmitt, 2019: Shapes and fall orientations of ice particle aggregates. *J. Atmos. Sci.*, **76**, 1903–1916, https://doi.org/10.1175/JAS-D-18-0251.1.

Kajikawa, M., 1982: Observations of the falling motion of early snow flakes. Part I. Relationship between the free-fall pattern and the number and shape of component snow crystals. *J. Meteor. Soc. Japan*, **60**, 797–803, https://doi.org/10.2151/jmsj1965.60.2_797.

——, and A. J. Heymsfield, 1989: Aggregation of ice crystals in cirrus. *J. Atmos. Sci.*, **46**, 3108–3121, https://doi.org/10.1175/1520-0469(1989)046<3108:AOICIC>2.0.CO;2.

Khvorostyanov, V. I., and J. A. Curry, 2002: Terminal velocities of droplets and crystals: Power laws with continuous parameters over the size spectrum. *J. Atmos. Sci.*, **59**, 1872–1884, https://doi.org/10.1175/1520-0469(2002)059<1872:TVODAC>2.0.CO;2.

——, and ——, 2005: Fall velocities of hydrometeors in the atmosphere: Refinements to a continuous analytical power law. *J. Atmos. Sci.*, **62**, 4343–4357, https://doi.org/10.1175/JAS3622.1.

Lawson, R. P., R. E. Stewart, and L. J. Angus, 1998: Observations and numerical simulations of the origin and development of very large snowflakes. *J. Atmos. Sci.*, **55**, 3209–3229, https://doi.org/10.1175/1520-0469(1998)055<3209:OANSOT>2.0.CO;2.

Lo, K. K., and R. E. Passarelli, 1982: The growth of snow in winter storms: An airborne observational study. *J. Atmos. Sci.*, **39**, 697–706, https://doi.org/10.1175/1520-0469(1982)039<0697:TGOSIW>2.0.CO;2.

Locatelli, J. D., and P. V. Hobbs, 1974: Fall speeds and masses of solid precipitation particles. *J. Geophys. Res.*, **79**, 2185–2197, https://doi.org/10.1029/JC079i015p02185.

Magono, C., and T. Nakamura, 1965: Aerodynamic studies of falling snowflakes. *J. Meteor. Soc. Japan*, **43**, 139–147, https://doi.org/10.2151/jmsj1965.43.3_139.

McFarquhar, G. M., M. S. Timlin, R. M. Rauber, B. F. Jewett, J. A. Grim, and D. P. Jorgensen, 2007: Vertical variability of cloud hydrometeors in the stratiform region of mesoscale convective systems and bow echoes. *Mon. Wea. Rev.*, **135**, 3405–3428, https://doi.org/10.1175/MWR3444.1.

Mitchell, D. L., 1988: Evolution of snow-size spectra in cyclonic storms. Part I: Snow growth by vapor deposition and aggregation. *J. Atmos. Sci.*, **45**, 3431–3451, https://doi.org/10.1175/1520-0469(1988)045<3431:EOSSSI>2.0.CO;2.

——, 1996: Use of mass- and area-dimensional power laws for determining precipitation particle terminal velocities. *J. Atmos. Sci.*, **53**, 1710–1723, https://doi.org/10.1175/1520-0469(1996)053<1710:UOMAAD>2.0.CO;2.

——, and A. J. Heymsfield, 2005: Refinements in the treatment of ice particle terminal velocities, highlighting aggregates. *J. Atmos. Sci.*, **62**, 1637–1644, https://doi.org/10.1175/JAS3413.1.

——, A. Huggins, and V. Grubisic, 2006: A new snow growth model with application to radar precipitation estimates. *Atmos. Res.*, **82**, 2–18, https://doi.org/10.1016/j.atmosres.2005.12.004.

Passarelli, R. E., 1978: An approximate analytic model of the vapor deposition and aggregation growth of snowflakes. *J. Atmos. Sci.*, **35**, 118–124, https://doi.org/10.1175/1520-0469(1978)035<0118:AAAMOT>2.0.CO;2.

——, and R. C. Srivastava, 1979: A new aspect of snowflake aggregation theory. *J. Atmos. Sci.*, **36**, 484–493, https://doi.org/10.1175/1520-0469(1979)036<0484:ANAOSA>2.0.CO;2.

Sasyo, Y., and T. Matsuo, 1980: On the statistical investigation of the fall velocity of snowflakes. *Pap. Meteor. Geophys.*, **31**, 61–79, https://doi.org/10.2467/mripapers.31.61.

Schmitt, C. G., and A. J. Heymsfield, 2010: The dimensional characteristics of ice crystal aggregates from fractal geometry. *J. Atmos. Sci.*, **67**, 1605–1616, https://doi.org/10.1175/2009JAS3187.1.

——, K. Sulia, Z. J. Lebo, A. J. Heymsfield, V. Przybo, and P. Connolly, 2019: The fall speed variability of similarly sized ice particle aggregates. *J. Appl. Meteor. Climatol.*, **58**, 1751–1761, https://doi.org/10.1175/JAMC-D-18-0291.1.

Seifert, A., U. Blahak, and R. Buhr, 2014: On the analytic approximation of bulk collision rates for non-spherical hydrometeors. *Geosci. Model Dev.*, **7**, 463–478, https://doi.org/10.5194/gmd-7-463-2014.

Szyrmer, W., and I. Zawadzki, 2010: Snow studies. Part II: Average relationship between mass of snowflakes and their terminal fall velocity. *J. Atmos. Sci.*, **67**, 3319–3335, https://doi.org/10.1175/2010JAS3390.1.

Thompson, P. D., 1968: A transformation of the stochastic equation for droplet coalescence. *Proc. Int. Conf. on Cloud Physics*, Toronto, ON, Canada, Amer. Meteor. Soc., 115–125.

Verlinde, J., P. J. Flatau, and W. R. Cotton, 1990: Analytical solutions to the collection growth equation: Comparison with approximate methods and application to cloud microphysics parameterization schemes. *J. Atmos. Sci.*, **47**, 2871–2880, https://doi.org/10.1175/1520-0469(1990)047<2871:ASTTCG>2.0.CO;2.

Vickers, G. T., 1996: The projected areas of ellipsoids and cylinders. *Powder Technol.*, **86**, 195–200, https://doi.org/10.1016/0032-5910(95)03049-2.

Walko, R. L., W. R. Cotton, M. P. Meyers, and J. Y. Harrington, 1995: New RAMS cloud microphysics parameterization. Part I:

The single-moment scheme. *Atmos. Res.*, **38**, 29–62, https://doi.org/10.1016/0169-8095(94)00087-T.

Westbrook, C. D., R. J. Hogan, and A. J. Illingworth, 2008: The capacitance of pristine ice crystals and aggregate snowflakes. *J. Atmos. Sci.*, **65**, 206–219, https://doi.org/10.1175/2007JAS2315.1.

Wisner, C., H. D. Orville, and C. Myers, 1972: A numerical model of a hail-bearing cloud. *J. Atmos. Sci.*, **29**, 1160–1181, https://doi.org/10.1175/1520-0469(1972)029<1160:ANMOAH>2.0.CO;2.

Wood, N. B., T. S. L'Ecuyer, A. J. Heymsfield, and G. L. Stephens, 2015: Microphysical constraints on millimeter-wavelength scattering properties of snow particles. *J. Appl. Meteor. Climatol.*, **54**, 909–931, https://doi.org/10.1175/JAMC-D-14-0137.1.

Zawadzki, I., E. Jung, and G. Lee, 2010: Snow studies. Part I: A study of natural variability of snow terminal velocity. *J. Atmos. Sci.*, **67**, 1591–1604, https://doi.org/10.1175/2010JAS3342.1.